國立交通大學

資訊工程學系
碩 士 論 文

腦磁波訊號源估測與同調性造影

Neuromagnetic Source Estimation and
Coherence Mapping of Brain Activities

研 究 生：鄭志瑜

指導教授：陳永昇　博士

中 華 民 國 九 十 四 年 八 月

Neuromagnetic Source Estimation and Coherence Mapping of Brain Activities

A dissertation presented

by

Chih-Yu Cheng

to

Department of Computer Science
and Information Engineering

in partial fulfillment of the requirements

for the degree of

Master of Science

in the subject of

Computer Science and Information Engineering

National Chiao Tung University

Hsinchu, Taiwan

2005

Neuromagnetic Source Estimation and Coherence Mapping of Brain Activities

摘要

　　腦磁圖儀非侵入地量測腦部活化源誘發出的磁場訊號。其能夠在高時間解析度的取樣下對腦部活化源做時空造影，利用此方式將可有助於人腦功能在臨床與基礎神經生理學方面的研究。在此論文之中，我們將提出新的空間濾波技術，其利用腦磁圖儀所量測的訊號記錄來估測腦中訊號源的顯著程度以及訊號源間的相關性。

　　利用磁圖儀所量測的紀錄來估算腦部活化源的問題稱之為逆估算問題。為了解此類的不適定問題，加入些假設與限制是需要的，例如等效電偶極的腦部訊號源模型、固定訊號源電偶極個數等假設以及結構性或是最小範數限制等。在眾多的訊號源逆估算方法中，光束構成法—一種空間濾波技術—在近十年來漸漸的引人注目。此訊號源逆估算法是藉由探測訊號源空間中一個接一個的體素，此時空間濾波器在每個位置會分別地被計算。此空間濾波器依據單位增益與最小變異量兩準則將可保留目標訊號源訊號並同時抑制其他訊號所造成的影響。然而，如何決定訊號源電偶極的方向會是個問題。在既有的文獻中主要提及三種方式，第一、此電偶極方向會垂直於該處大腦皮質表面，然而自動地且精確地重建出曲折的皮質表面是非常困難的；第二、利用搜尋的方式找出，但此方法是非常耗時的；第三、將訊號源電偶極拆解成三個互成正交的分量，但其有遺漏偵測的風險。

　　此論文中，我們開發了一個新空間濾波技術，稱之為最大對比光束構成法，用以對神經訊號源做統計量的造影。除了如同傳統的光束構成法一樣的採用單位增益與最小變異量準則，我們所提的方法還利用了最大對比（活化與休息狀態逆估算出的神經活化訊號變異量的比值）準則。藉由此最大對比準則，我們將可用閉形式解的方式解析地決定出訊號源電偶極方向，也就是說，對於某一位置而言，能夠有效率地得出其對應的空間濾波器。一旦藉由對腦磁圖儀所量測訊號濾波所估算出各個位置的訊號源，將可計算對應整個訊號源空間的 F 統計量以視覺化在活化狀態時於皮質區的訊號源相對應於休息狀態的顯著程度。

　　同調性訊號源造影是另一個在人腦功能研究上有趣的主題，其能有助於探索人腦相關功能區域間聯繫的機制。近來，在特殊頻帶下的同步震盪訊號被認為與神經網路間的溝通有著密切的關係。同調訊號源造影法利用光束構成法為基礎，對相對於一參考訊號擁有同調性的皮質區訊號源做造影。但其僅適用於同步頻帶具有穩恆的特性。在此，我們提出另一新技術—最大正規化相關光束構成法—利用最大正規化相關性的準則解析地且閉形式的決定訊號源方向以對同調訊號源造影。理論上，此方法是一般化的，也就是它能對在任一有定義自相關性與互相關性的定義域中互有相關性的訊號作造影。此論文中，我們在感興趣的 Morlet 小波域中計算腦磁波儀所量測訊號的自相關性以及其與參考訊號的互相關性，接著利用所提出的最大正規化相關光束構成法來對動態跨頻同調訊號源造影。

　　模擬、假體以及手指抬動的實驗被採用來驗證與評估所提方法的正確性與能力。根據模擬與假體實驗所得的分析結果，我們的方法的確，第一、能既有效率地並準確地決定出訊號源電偶極的方向；第二、能準確地分別定位出擁有顯著變異量與時頻同調性的訊號源。當應用在手指抬動的實驗分析時，我們可從 F 統計量圖明顯的指出在腦部感覺運動區在活化狀態相對於休息狀態有高度的對比。

Abstract

Magnetoencephalography (MEG) non-invasively measures the electromagnetic signals induced by brain activities. It can provide spatiotemporal brain activation imaging with high temporal resolution to facilitate functional brain research in both clinical and basic neuroscience fields. In this thesis, we propose novel spatial filtering techniques for statistical mapping of neuronal sources as well as cortical oscillatory coupling by using the whole-head MEG recordings.

The problem of estimating the activation sources in the brain from the MEG recordings is called the inverse problem. To solve this ill-posed problem, approximations such as equivalent current dipole for source modeling, assumptions such as a fixed number of dipoles during the task, and constraints such as anatomical constraint and minimum-norm constraint are required to limit the solution space. Among the various kinds of source estimation methods, beamforming technique, a kind of spatial filtering technique, has becoming more and more attractive during the past decade. By probing the source space in a voxel-by-voxel manner, a spatial filter is individually calculated for each position. This spatial filter can reconstruct the activation magnitude of the targeted source while suppressing the contribution from other sources by imposing the unit-gain constraint and by applying the minimum-variance criterion. However, the determination of dipole orientation can be problematic. There are three major kinds of methods proposed in the literature. First, the dipole orientation is aligned to be perpendicular to the cortical surface. Unfortunately, the surface reconstruction for the convoluted cortex is very difficult and the reconstruction deviation will decrease the accuracy of the orientation. Second, the dipole orientation is determined by (exhaustive) search, which is time-consuming. The third kinds of methods decompose the dipole into three orthogonal components, which may suffer the risk of miss-detection.

In this work, we develop a novel spatial filtering technique, called the maximum-contrast beamformer, for statistical mapping of neuronal sources. In addition to the unit-gain constraint and the minimum-variance criterion, as in the conventional beamformers, our method exploits a maximum-contrast criterion that can maximize the discrimination between the estimated neuronal activities in the active state and those in the control (or

resting) state. The maximum-contrast criterion helps to analytically determine the dipole orientation in a closed-form manner and the spatial filter can be obtained very efficiently for each targeted position. Once the neuronal activity waveform is estimated in the source space by spatially filtering the MEG recordings, F-statistic map can be calculated to reveal cortical regions with significant difference of activities between the control and active states.

Another interesting issue in functional brain studies is the coherent source mapping for probing the binding mechanism of connected functional assemblies. Recently, oscillatory synchronization in particular frequency bands has been shown to be closely related to the communication within a neural circuit. By using the beamforming-based algorithm, DICS (Dynamic Imaging of Coherence Source) method can map the cortical sources that are statistically coherent to a specified reference at a certain frequency band. The limitation of the DICS method is that the synchronization frequency band is considered to be stationary during the task. Here, we propose another new method, maximum-normalized-correlation beamformer, for the mapping of the cortical oscillatory coupling. Theoretically, this method is very general that can image the sources correlated in the domain where the autocorrelation and crosscorrelation can be defined. To demonstrate the capability of this method, we compute the autocorrelation and crosscorrelation for the MEG recordings in the Morlet wavelet domain and image the dynamic coherent sources across multiple frequency bands during the task. Moreover, the dipole orientation has a closed-form solution by applying the maximum-normalized-correlation criterion.

Experiments with simulation, phantom, and real data are conducted to verify the correctness and to assess the capability of the proposed methods. According to the experiments with simulation and phantom data, our methods indeed can efficiently and accurately calculate the dipole orientation. Also, our methods correctly locate the sources with significant variance and significant time-frequency coherence. When applied to a finger-lifting study, F-statistic map computed from the estimated neuronal activities on the cortical surface clearly identify the sensorimotor area with high contrast.

誌謝

　　本篇論文得以完成，首先要誠摯的感謝自小到大花費無盡心血栽培我的父母親。有他們在背後的支持，我才得以完成此碩士學位。再則，感謝我的指導教授陳永昇老師以及陳麗芬老師，在這兩年多來引領我如何做研究，並對於我的論文提出了許多寶貴看法與意見。他們所給予的助益，是本篇論文完成的直接重要因素。最後，感謝實驗室的同儕們，在這段日子以來，對我直間或間接的幫助。

Contents

List of Figures

List of Tables

Chapter 1

Introduction

1.1 Backgrounds

In the past three centuries, the development of technology is more and more flourishing and the world rapidly change in this era. For instance, light has replaced candle to light in night, car has replaced horse-drawn vehicle to transport goods, abacus has been replaced by electric calculator to do accounts and even the computer equipping artificial intelligence could beat all humans on chess table. Almost every thing around our life is greatly effected by this technology progressing.

Human knows the principles of nature to create those mentioned above. From the theory of mechanism, heats to electromagnetism, human beings create textile, steam machine and motor. Medical science brings the better prevention of and treatment of disease to extend humans' lift. Agriculture science brings more quantity of output to supply the increasing population. Aeronautical science make the dream of fling come true by the appearance of airplane. Many people donate on each field to think and develop new methods or tools to push the era forward.

All ideas of those principles and invents come from a powerful device, human brain. Human brain is often analogized with the most powerful computer. That brain controls hands, feet, eyes and most organs is like that the control unit in the central processing unit (CPU) coordinates memory, peripheral devices in the whole computer system. Brain processes the information receiving by eyes, ears, nose resembles that the arithmetic/logic unit (ALU) in CPU processes the information which inputs through keyboard and mouse. Also, brain supports parallel processing so that we can read the news on web, press the mouse button, drag it to scroll the page, listen music and follow the melody to hum the tune simultaneously. Besides, brain wins the computer in several aspects. The most advantage of human brain is that it owns the originality being able to cerate infinite possible, whereas the computer is just a deterministic machine. Moreover, it could perform so many functions but its size is magically small. "Deep blue" that is match for the best human player on chess weights 1.4 ton about 1000 times of the matured human brain, whereas it is just able to chess. Human brain is what a dedicate device!

Of course that there is no reason that no one has interest to know the mechanism of the operations in this mystical and attractive device. From many centuries ago, the studies
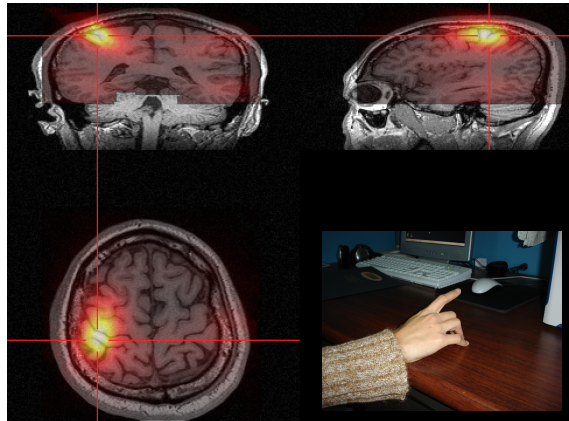
Figure 1.1: A finger lifting example about brain functional mapping. When we perform a certain functional task, the corresponding cortex areas in the brain will activate. From sagittal, coronal and transverse view, the figure shows significance of the average power of the estimated signal by beamforming-based method using MEG recordings. It evidently shows that the sensorimotor area activates during the period of finger lifting.

on brain started form the anatomy to explore the structure of it. Then, in the later of nineteen century, the electric brain signal was found. Through the researches in early and mid twenty century, it was more and more clear that when we perform a certain task, the neurons at the corresponding cortex area in the brain will activate. The activation is the electrical signals resulting from the irons flowing in and out the cells of the neurons to perform the information interchange between the neurons. For instance, when we look at something, the neurons in the visual cortex area, at the occipital part of the brain will activate. Figure 1.1 gives another example that sensory and motor areas activate when we lift our finger up.

However, comparing with other technologies, the functionality of the human brain is still a virgin land to scientists. We still have few idea about our brain yet. It is very difficult to explore the human brain because of the extraordinary sophistication and complexity of it, which consists of billions of micron-sized neurons connecting with each other to knit a very complex neural network for performing many works. Besides, due to morality, there are many limitations of the researches on living bodies. For instance, it can not force an ordinary one to be incised his scalp to denoting his brain for studies. Hence, the progress

of the studies on the field of functionality of the human brain is comparatively slow.

Today, by the progress of the technologies in both hardware and software, there are many useful instrumentations can help us to explore the functionality of human brain more accurate and more convenient, even some can under the non-invasive condition, that is, during the experiment, there is no physical harm to the subject. Now, for non-invasively studying on brain functionality, there are three primary modalities, which are functional magnetic resonance imaging (fMRI), electronic encephalograph (EEG) and magnetic encephalograph (MEG). All of these three receives the brain signal outside the head by sensors and can be think that they take the picture for the phenomena caused by the brain electrical activities. fMRI is a widely-used device measuring the changes in blood oxygenation which is related to the neural activities. It has the advantage of high spatial resolution, but with the disadvantage of low temporal resolution. EEG and MEG directly measure the electrical potential and induced magnetic filed caused by the iron flow respectively. Besides, they own the ability to measure the signal with high temporal resolution up to the order of millisecond.

Temporal resolution of the instructions for the studies of brain functionality is important. Because, the the brain activities could dynamically change up to about $70 \sim 80$ Hz, that is, by the Nyquist sampling theorem [50], the sampling frequency at least needs about 160 Hz to reconstruct the origin signals. In addition, recently, more and more studies direct that the large-scale integration in the brain is done by the information involving in the frequency domain of the signals [3, 4, 56, 64, 67, 71]. For a functional task, there are not only the primary but other regions associating with it. It is the ensemble functionality of the involved neural network that achieve this task. For example, when we lift our finger up, the regions corresponding visual, auditory, dorsolateral prefrontal association, somatosensory and motor cortex may be involved. How those spatially-distributed regions know that they cooperate in the same job is so called large-scale integration problem, or say binding problem. Although there is still no concrete answers to the problem, the most plausible candidate is by the modulation of the wave with certain frequency bands. The concept is illustrated in the Figure 1.2. For these reasons, EEG and MEG plays indispensable roles for the study of brain connectivity because they are with the ability of high temporal resolution. Figure 1.3 illustrate the acquisition of EEG and MEG recordings.
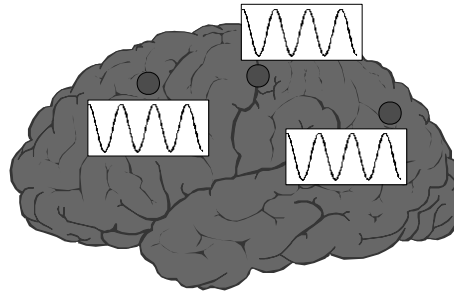
Figure 1.2: Large scale integration problem. When performing a certain task, several cortex areas (circle) may be involved. Cooperation mechanism of these involved cortex areas is still in debate. However, more and more studies consider that the most possible candidate is the rhythm which modulates the signals generated by the cooperated cortex ares. Thus, those signals are correlated in the certain frequency band(s) and are called as coherent sources.

Nevertheless, not only low signal to noise ratio (SNR) but also ill-posed inverse problem are two major difficulties in the studies of brain functionality by the modality of EEG or MEG. First, the scale of the brain electrical signals is very small compared to the environmental noise and confoundings. For example, the magnitude of the induced magnetic field is around $10^{-13} \sim 10^{-15}$ Tesla while the omnipresent earth's static filed is about 10^{-5} Tesla (Tesla is the unit of magnetic field). Hence, both a proper environment for experiment and the signal preprocessing before analyzing or further processing are necessary. Second, the recordings on EEG/MEG sensors are not induced by a single source but are the superpositions of the contributions induced by sources distributed all over the brain. It can be considered as that we set some microphones for recording the voice in a clamorous cocktail party and hence each microphone will record the mixture of the voice from all the people in the party rather than an individual one. Although there are many researches based on EEG or MEG modalities directly analyze the recordings, they may have bias due to the mixed effect. The problem of estimating the individual signal of each source from the EEG or MEG recordings measured outside the scalp is called the inverse problem. Shown by Helmholtz (1853), the difficulty in solving the problem is that it mathematically is an ill-posed problem which has no unique solution but infinite. That is, we can not solve it easily.
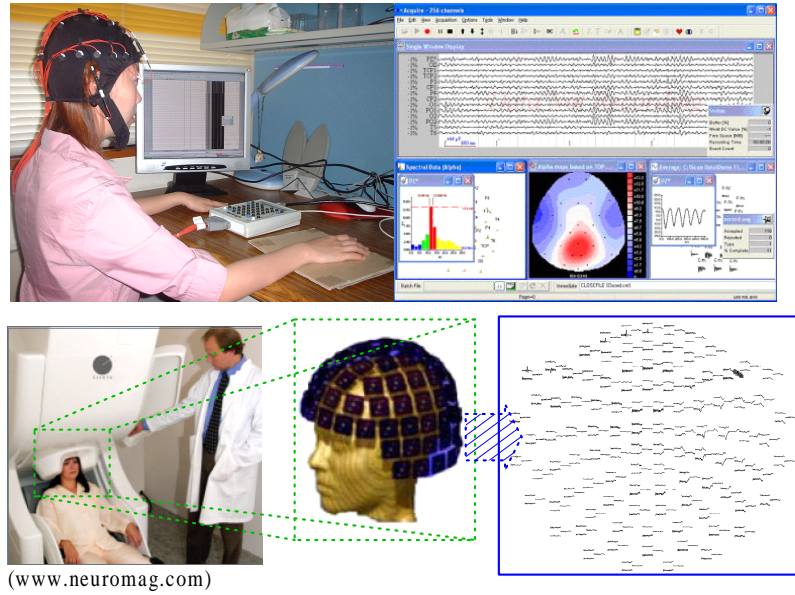
Figure 1.3: Acquisition of the electric and induced magnetic signals by EEG and MEG. The upper and lower parts respectively are for EEG and MEG. Both of they acquire the time course recordings by several sensors locating outside the scalp with the sampling rate up to the order of kilo-Hz. Due to such high temporal resolution property, they are adaptive to be the modalities for the studies on brain functionality.

Before describing the individual algorithms for solving the inverse problem, it needs to know that the concepts of most algorithms involve the Bayesian statistic framework:

$$P(x|y) = \frac{P(x)P(y|x)}{P(y)}. \tag{1.1}$$

$P(x|y)$ denotes the conditional probability of x given y while $P(x)$ and $P(y)$ are the probability of x and y respectively. $P(y|x)$ denotes the conditional probability of y given x. Applying to MEG inverse problem, let x be the parameters of the sources in the head and y be the recordings on the sensors such that $P(x|y)$ describes the inverse problem. The Bayesian equation shows that if we want to know the source parameters by the recordings, we can transform the problem to the form at the right side of the equal sign. Thus, knowing $P(y|x)$ is a necessary condition. $P(y|x)$ describes the probability of the recordings when given the source parameters, that is, the forward problem, which has the unique solution when we know the electric source and head (conductor) model. The problem and its solution will be briefly describes in Chapter 2. Figure 1.4 illustrates forward, inverse problem
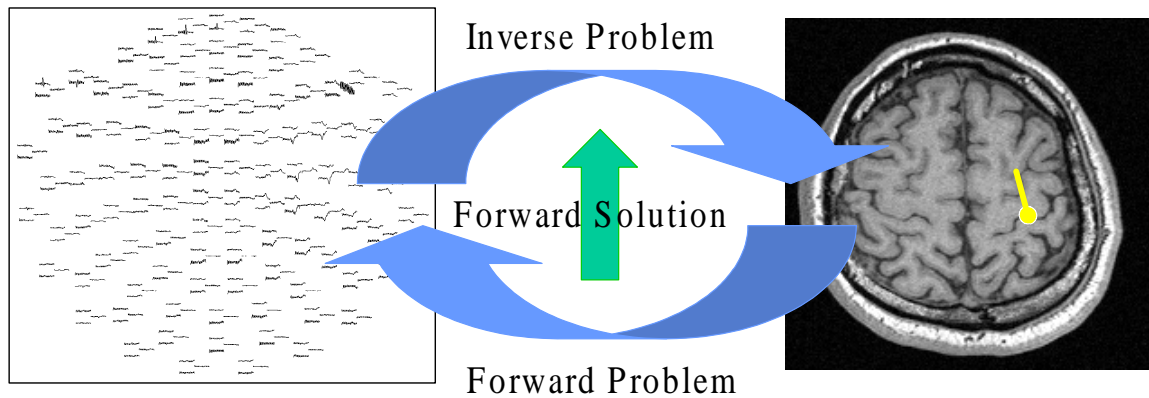
Figure 1.4: Forward and inverse problem and their relationship. Given a putative source in the brain, what the magnetic field distributes outside the head is the forward problems (right to left). Oppositely, the inverse problem describes how we reconstruct the brain sources by the recordings on sensors outside the head (left to right). To solving the inverse problem is always involving the solution of the forward problem which has the unique solution when we knows the electric source (light green arrow) and head (conductor) model.

and their relationship.

As aforementioned, the inverse problem has infinite solutions; hence, several algorithms based on various constraints were been developed in the literatures to derive a unique solution for the problem. These algorithms can be roughly divided into primary two categories that think a source as a focal current or distributed currents respectively. These two assumptions are both reasonable, because we can find a group of distributed currents that effect the same contribution to the EEG/MEG recordings with a specific focal current, and vice versa. The representative algorithms in first category is based on dipole modeling and spatial filter. The dipole modeling method is a nonlinear searching method to determine the parameters of the given number sources, the least square dipole fitting algorithm [27, 30, 49, 58] is an example. The spatial filter method estimates the source by linear combining the recordings measured by sensors. The coefficients for the linear combination are adaptively determined by different criteria in different algorithms. Beamforming [22, 54, 59, 72] and multiple signal classification (MUSIC) [46, 48] algorithms are the examples. The other category assumes the sources is the distributed currents and the minimum norm estimation (MNE) [26, 43] method belongs to it.

Solving the inverse problem and visualizing the results can be think as the imaging process for the brain signals. That is, after applying the inverse procedure on the recordings, we can "see" the (estimated) activities in the brain. For the studies of the basic functional brain mapping, imaging where the source current magnitude (power) is significant gives the direct information reflecting the activation of the neurons there. Most inverse algorithms have proposed in the literatures belongs to these category. For another interesting and mystical problem, the binding problem, studies often exploit a measurement, "coherence", to quantify the connective level between different neural groups distributed in the brain. It results from that, as aforementioned, several studies reveals that the cooperative neural groups may share the modulation in certain frequency bands, such that the statistic in these bands should be similar between those groups and therefore coherence which is a measurement to judge the similarity of the signals in frequency domain is a proper media to implicitly point out the significance of the connective likelihood of those neural groups. Recently, some inverse algorithms, like [13, 20, 22, 31], were developed to image the coherent level of the (estimated) brain sources under a narrow frequency band. Besides, Sun et al. [66] and Sekihara et al. [61, 63] respectively presented methods based on least square dipole fitting approach and MUSIC involving the time-frequency representation to estimate the brain sources which best match the specified the time-frequency behaviors.

1.2 Thesis Scope

In this thesis, we focus on beamforming-based algorithm for solving inverse problem with MEG modality. The advantage of beamforming-based algorithm will be described at the first section of Chapter 3. Besides, though most algorithms or procedures associating MEG are still suitable for EEG, we choose MEG be the modality here due to first, the SNR of the recordings usually is higher than EEG and, second, the forward solution can be derived by a simpler way with sufficient accuracy simultaneously.

Beamforming-based inverse algorithm, or say beamformer, is the spatial filter, which can be think as putting a virtual sensor on a specific position with a specific direction to probe the source there according to the criteria of minimizing total variance of the esti-

mated source and retaining unit gain to the specific position and direction. Theoretically, everywhere and every orientation in the brain is need to be probed for imaging the activities distributing over the whole brain. However, it is impossible due to the computational limitation. For the end of overcoming the problem, sampling the position space is adopted and the sampling rate is dependent on the desired spatial resolution. However, at one position, it just needs to determine a direction matching the orientation of the source there to be probed. Linearly constrained minimum variance spatial filter proposed by Van Veen et al. [72] samples the orientation solution space with three probing directions which are orthogonal with each other. Consequently, it sums of the results probed on the three directions and views the summation as the estimated result. However, because the intrinsic property, unit gain constraint and minimum variance, of the beamforming-based algorithm, sampling will flat the source distribution, even miss the detection of the source in the extreme condition. Robinson and Vrba proposed a method, called "synthetic aperture magnetometery" (SAM), [54] which searches the optimal orientation according to the maximum z-statistic criterion. They also show the resultant distribution of the estimated brain signal is more focal by SAM than LCMV especially when the SNR is high [73]. The major drawback of SAM is that the computational cost is heavy.

Besides, almost studies about sources coherence for the binding problem analyzed the MEG/EEG recordings directly, like [1,32,35,38,39,57], but Gross et al. [22] proposed "dynamic imaging of coherent sources (DICS)" method which is yet the only beamforming-based inverse algorithm, to image the coherent sources. It performs in a narrow frequency band when given a reference signal. The method determines the source orientation by find the principle axis (maximum correlation) in this orientation solution space.

For the sake of overcoming the tradeoff between computational cost and resultant accuracy in the issue of determining the source orientation , in this thesis, we propose two new beamforming-based algorithms for imaging the source significance and coherent sources respectively. Also, we apply the later method to image the time-frequency coherent sources for an extension of DICS. The term, time-frequency coherence, describes that the coherent frequency of two sources are not limited in a narrow band but may cross two or several bands with time, that is, in time-frequency domain. In the following, we briefly describe the two beamforming-based algorithms and the imaging method of the time-frequency co-

herent sources proposed in this thesis.

I. Maximum contrast beamformer Maximum contrast beamformer is a beamforming-based algorithm to image the source significance by MEG/EEG recordings with the properties both of efficiency and no probability of miss-detection. It still follows the minimum variance and unit gain constraint criteria as conventional beamforming-based algorithms to solve the MEG inverse problem, but the source orientation is determined by maximum contrast criterion with a deterministic computational steps.

II. Maximum normalized correlation beamformer Maximum normalized correlation beamformer is a beamforming-based algorithm to image the correlated sources with a given reference signal by MEG/EEG recordings with the properties both of efficiency and no probability to miss-detection. It still follows the minimum variance and unit gain constraint criteria as conventional beamforming-based algorithms to solve the MEG inverse problem, but the source orientation is determined by maximum normalized correlation criterion with a deterministic computational steps. Theoretically, it is able to image the correlated sources not only in the frequency domain but also in any domain that the auto- and cross-correlation have been defined.

III. Imaging the time-frequency coherence We apply the proposed beamforming methods to image the coherent sources cross different frequency bands with time. by computing the auto- and cross-correlation of the selected wavelet coefficients both of one (estimated) targeted signal and one reference signal.

In this work, we implemented the proposed methods in C/C++ language on Win32 platform. The simulation and phantom experiments are conducted to input theirs recordings into the proposed algorithm for verification and demonstration. We also apply our methods to the recordings recorded from real finger lifting experiments.

1.3   Thesis Organization

After this chapter, we start to introduce the forward problem and its solution for the preparation for the inverse algorithms described later. Consequently, in Chapter 3, af-

ter introducing some typical inverse algorithms first and mentioning the advantage of the beamforming-base method, we elaborate the basic of beamformer for imaging the source significance. Next, the aforementioned drawbacks of LCMV and SAM are pointed out more detail respectively before we propose the maximum contrast beamforming method with the detail deduction. Then, the principles of the DICS and maximum normalized beamforming method which image the coherent sources are expounded in order. At the end of that chapter, we describe the procedure for imaging the time-frequency coherent sources. Chapter 4 consists of the results of the experiment for the verification and demonstration of the proposed methods. Finally, a short conclusion for the thesis is given at the last chapter.

Chapter 2

MEG Forward Prediction with Spherical Head Model

According to the Bayesian statistic framework mentioned in last chapter, the inverse algorithms have to involve the forward solution to estimate the parameters of the brain sources when given the recordings measured by MEG sensors. Therefore, we need to, at first, construct the MEG forward model which describes the distribution of the the magnetic field outside the head when giving putative current sources in the brain. The general forward model can be deduced from quasi-static Maxwell equation and Biot-Sarvas law; however, in one hand, to analyze the brain behavior to the neuron-sized level is very difficulty; in the other hand, there is no analytical solution for the general form forward model, but needs to be computed numerically.

In the MEG-related studies, it usually uses equivalent current dipole (ECD) to approximate the total electromagnetic effect caused by a group of neighboring neurons such that we can microscopically view the neurons' activities for simplification. Besides, the spherical head model is often adapted for deriving an analytical solution of the forward model to reduce the computational cost. In the following, we will briefly introduce the forward problem from the general model, ECD source model, the spherical head forward model to, finally, the formulation of deriving the MEG recordings when giving sources.

2.1   General Forward Model

The frequency band of almost interesting bio-electromagnetic signals are under 100Hz. At this condition, the physics of MEG can be described by quasi-static Maxwell equation [27]. Under this assumption, when a current density $\eta(\mathbf{r}_\eta)$ locates at $\mathbf{r}_\eta$ in a closed volume G, the magnetic field $\mathbf{b}(\mathbf{r})$ at location $\mathbf{r}$ outside G can be described by the well-known Biot-Sarvas law

$$\mathbf{b}(\mathbf{r}) = \frac{\mu_0}{4\pi} \int_G \eta(\mathbf{r}_\eta) \times \frac{\mathbf{r} - \mathbf{r}_\eta}{\|\mathbf{r} - \mathbf{r}_\eta\|^3} \, d\mathbf{r}_\eta, \tag{2.1}$$

where μ_0 is the permittivity of free space. The overall current density can be view as the sum of two components, passive and primary parts. In our case, the primary currents $\eta_\mathbf{p}(\mathbf{r}_\eta)$ associates the original neural activity, and the passive part, or say volume current $\eta_\mathbf{v}(\mathbf{r}_\eta)$, is the result of the the induced potential of the conducting medium. The relation can be

formalized as

$$\eta(\mathbf{r}_\eta) = \eta_{\mathbf{p}}(\mathbf{r}_\eta) + \eta_{\mathbf{v}}(\mathbf{r}_\eta) = \eta_{\mathbf{p}}(\mathbf{r}_\eta) + \sigma(\mathbf{r}_\eta)\mathbf{e}(\mathbf{r}_\eta) = \eta_{\mathbf{p}}(\mathbf{r}_\eta) - \sigma(\mathbf{r}_\eta)\nabla\mathbf{v}(\mathbf{r}_\eta), \qquad (2.2)$$

where $\mathbf{e}(\mathbf{r}_\eta)$ is the electric field that equals the negative gradient of the electric potetial $\mathbf{v}(\mathbf{r}_\eta)$, and $\sigma(\mathbf{r}_\eta)$ is the conductivity of the mediums which indicates the brain tissues in our case.

Typically, the head can be think include three to five regions, for example, scalp, skull, cerebrospinal fluid, gray matter and white matter [47]. Moreover, the conductivity of each are considered constant and isotropic such that the Biot-Sarvas law can be rewritten as the sum contributed by the primary and volume currents:

$$\mathbf{b}(\mathbf{r}) = \mathbf{b_0}(\mathbf{r}) + \frac{\mu_0}{4\pi}\sum_{ij}(\sigma_i - \sigma_j)\int_{S_{ij}}\mathbf{v}(\mathbf{r}_\eta) \times \frac{\mathbf{r} - \mathbf{r}_\eta}{\|\mathbf{r} - \mathbf{r}_\eta\|^3}\,d\mathbf{S}'_{ij}, \qquad (2.3)$$

where σ_i and σ_j are the conductivities of the successive mediums. The second term at the right of the equal sign is the magnetic contribution from the volume currents formed by summing the integrating over the cross-medium surface $\mathbf{S}'_{ij}$, eg. scalp-skull, gray-white matter, and so on. The first term is the primary magnetic field:

$$\mathbf{b_0}(\mathbf{r}) = \frac{\mu_0}{4\pi}\int_G \eta_{\mathbf{p}}(\mathbf{r}_\eta) \times \frac{\mathbf{r} - \mathbf{r}_\eta}{\|\mathbf{r} - \mathbf{r}_\eta\|^3}\,d\mathbf{r}_\eta \qquad (2.4)$$

which is the magnetic field contributed by primary source only and the corresponding primary potential field is

$$\mathbf{v_0}(\mathbf{r}) = \frac{1}{4\pi\sigma_0}\int_G \eta_{\mathbf{p}}(\mathbf{r}_\eta) \cdot \frac{\mathbf{r} - \mathbf{r}_\eta}{\|\mathbf{r} - \mathbf{r}_\eta\|^3}\,d\mathbf{r}_\eta \qquad (2.5)$$

We need to know that the potential on all surfaces of mediums for deriving a general equation describing the magnetic field. By Green's theorem, the relation of the potential at $\mathbf{r}$ and the potential of the source can be formulated [58] [47] as

$$(\sigma_i + \sigma_j)\mathbf{v}(\mathbf{r}) = 2\sigma_0\mathbf{v_0}(\mathbf{r}) - \frac{1}{2\pi}\sum_{ij}(\sigma_i - \sigma_j)\int_{S_{ij}}\mathbf{v}(\mathbf{r}_\eta) \times \frac{\mathbf{r} - \mathbf{r}_\eta}{\|\mathbf{r} - \mathbf{r}_\eta\|^3}\,d\mathbf{S}'_{\mathbf{ij}}. \qquad (2.6)$$

Up to now, if the parameters of head is known, we can substitute Eq. (2.4) and Eq. (2.6) into Eq. (2.3) to solve the forward problem, that is, when given a source inside the head, we can derive the magnetic field anywhere outside the scalp, under the assumption of quasi-static magnetic field computation and that of constant isotropic conductivity of the homogeneous regions in the brain. However, the solution, in general, is not analytical and need to be solved numerically.

2.2   Source Model

According to the knowledge of neural-physiology, the active large pyramidal neurons locating at gray matter gives the primary contribution to the MEG recordings owing to two primary reasons. First, these neurons arranged at a regular direction which is perpendicular to the cortical surface so the contribution from each neuron will not be canceled out like other disorderly-arranged neurons. Second, the duration of the electrical signal at this place is more longer than others [2] such that the integration of their power is larger enough to be measured.

Although the actual electric activities take place within each neuron, we always model the activities from a macro view. It is owing to the fact that, first, a large number of neighbor neurons activate together and that, second, it is very difficult to study the neuron activities finely to the neural level with the device like MEG which equips rather few number of sensors compared with the number of the neurons. Hence, for convenience and simplicity, a small patch of activated cortex centralized at $\mathbf{r}'$ is considered and the primary current density can be approximately represented by the current dipole representation which is called equivalent current dipole (ECD) with the parameters of position, orientation and magnitude. Thus, we can view the large numbers of activated neurons as a point of dipole source:

$$\eta_{\mathbf{p}}(\mathbf{r}_\eta) = \mathbf{q}\delta(\mathbf{r}_\eta - \mathbf{r}'), \tag{2.7}$$

where δ is the Dirac delta function and the $\mathbf{q}$ is the dipole moment defined by

$$\mathbf{q} = \int \eta_{\mathbf{p}}(\mathbf{r}_\eta)\, d\mathbf{r}_\eta. \tag{2.8}$$

With the dipole moment representation, Eq. (2.4) and Eq. (2.5) can be respectively simplified as

$$\mathbf{b_0}(\mathbf{r}) = \frac{\mu_0}{4\pi}\mathbf{q} \times \frac{\mathbf{r} - \mathbf{r}'}{\|\mathbf{r} - \mathbf{r}'\|^3}, \tag{2.9}$$

$$\mathbf{v_0}(\mathbf{r}) = \frac{1}{4\pi\sigma_0}\mathbf{q} \cdot \frac{\mathbf{r} - \mathbf{r}'}{\|\mathbf{r} - \mathbf{r}'\|^3}. \tag{2.10}$$

2.3 Forward Solution for Spherical Head Model

For the sake of computing the solution for the forward problem formulated as Eq. (2.3), the information of the head is needed in advance. Realistic head model can be derived by segmenting the surface of each tissue on the volume image scanned by X-ray computed tomography (CT) imaging or magnetic resonance (MR) imaging instruments. Then, the forward solution can be calculated by finite element method (FEM) or boundary element method (BEM) [15]. However, calculating the solution by both of these methods are time-consuming because they have to solve the problem numerically.

A spherical head model is a simple model of the head with the advantage of fast computing for forward problem and also retains an acceptable accuracy to the MEG applications [2, 47]. The model assumes the head be comprised by a set of nested concentric spheres. At this condition, an analytical forward solution can be derived and the accuracy has be verified by the phantom dipole fitting experiments which shows there is no great effect to the result of source localization by MEG recordings [37]. At the following paragraph, it will describe the forward solution under the spherical head assumption.

Involving the sphere head model, it divides the magnetic field $\mathbf{b}(\mathbf{r}')$ into two parts, radial and tangential components, the direct of which are radial and tangential to the sphere surface respectively. The radial component of the magnetic field at $\mathbf{r}$ can be compute as

$$\mathbf{b_r}(\mathbf{r}) = \mathbf{b}(\mathbf{r}) \cdot \frac{\mathbf{r}}{\|\mathbf{r}\|}, \tag{2.11}$$

where $\|\mathbf{r}\|$ is the magnitude of $\mathbf{r}$. Because $\mathbf{r}/\|\mathbf{r}\|$ is the normal direction of the sphere surface, it can be found that the term in Eq. (2.3) caused by volume current will varnish. That is, the $\mathbf{b_r}(\mathbf{r})$ are just effect by the primary current:

$$\mathbf{b_r}(\mathbf{r}) = \mathbf{b_0}(\mathbf{r}) \cdot \frac{\mathbf{r}}{\|\mathbf{r}\|} = \frac{\mu_0}{4\pi} \left(\mathbf{q} \times \frac{\mathbf{r} - \mathbf{r}'}{\|\mathbf{r} - \mathbf{r}'\|^3} \cdot \frac{\mathbf{r}}{|\mathbf{r}|} \right) = \frac{\mu_0}{4\pi} \mathbf{r} \times \mathbf{r}' \cdot \frac{\mathbf{q}}{\|\mathbf{r}\|\|\mathbf{r} - \mathbf{r}'\|^3}. \tag{2.12}$$

The last equality above is due to $(\mathbf{a} \cdot \mathbf{b}) \times \mathbf{a} = \mathbf{a} \times \mathbf{b}$. This shows if the normal direction of the sensors is radial to the sphere surface, Eq. (2.12) is the solution. Oppositely, when the direction is not radial, tangential components which includes the effects of volume current must be considered. However, Sarvas [58] shows it has no necessary to explicitly compute the term associating volume currents. It exploits the radial magnetic field $\mathbf{b_r}(\mathbf{r})$ to derive a

magnetic potential $u(\mathbf{r})$ and then derive the full magnetic potential outside the head volume by the relation $\mathbf{b}(\mathbf{r}) = -\mu_0 \bigtriangledown u(\mathbf{r})$. Summarizing form of the magnetic field outside the head sphere according to the Sarvas model is

$$\mathbf{b}(\mathbf{r}) = \frac{\mu_0}{4\pi F^2(\mathbf{r}, \mathbf{r})} F(\mathbf{r}, \mathbf{r}) \mathbf{q} \times \mathbf{r}' - (\mathbf{q} \times \mathbf{r}' \cdot \mathbf{r} \nabla F(\mathbf{r}, \mathbf{r})), \qquad (2.13)$$

where ∇F is the gradient of the scalar function F which is

$$F(\mathbf{r}, \mathbf{r}') = \|\mathbf{r} - \mathbf{r}'\|(\|\mathbf{r}\|\|\mathbf{r} - \mathbf{r}'\| + \|\mathbf{r}\|^2 - (\mathbf{r}' \cdot \mathbf{r})). \qquad (2.14)$$

Mosher et al. [47] rearrange the solution of forward problem which utilizes the spherical head model to a pretty form by separating the linear and nonlinear parts of the dipole parameters. This reduces the computational cost for solving the inverse problem in practice, because the linear parameter has no necessary to find numerically. This form can be represented as

$$\mathbf{b}(\mathbf{r}) = \mathbf{K}(\mathbf{r}, \mathbf{r}') \cdot \mathbf{q}, \qquad (2.15)$$

where $\mathbf{q}$ concludes the amplitude and orientation information of the dipole, whereas the parameter of dipole position is nonlinearly involved in the kernel matrix $\mathbf{K}(\mathbf{r}, \mathbf{r}')$. For the case of Sarvas model in Cartesian coordinate system,

$$\mathbf{K}(\mathbf{r}, \mathbf{r}') = [\frac{\mu_0}{4\pi} \frac{\nabla F \mathbf{r} - F \mathbf{I}}{F^2} \mathbf{C}_{\mathbf{r}'}], \qquad (2.16)$$

where $\mathbf{C}_{\mathbf{r_q}}$ equals

$$\begin{pmatrix} 0 & -r'_z & r'_y \\ r'_z & 0 & -r'_x \\ -r'_y & r'_x & 0 \end{pmatrix}$$

and $\mathbf{r}' = [\begin{pmatrix} r'_x & r'_y & r'_z \end{pmatrix}]^T$. Figure 2.1 gives a depiction of the elementary elements and their relationship in the MEG forward model with spherical head model. When there are more than one sources, the resultant magnetic field is the sum of the effect by each individual source. That is,

$$\mathbf{b}(\mathbf{r}) = \sum_{\forall i} \mathbf{K}(\mathbf{r}, \mathbf{r}'_i) \cdot \mathbf{q}_i, \qquad (2.17)$$

where i denotes the number of the dipoles.
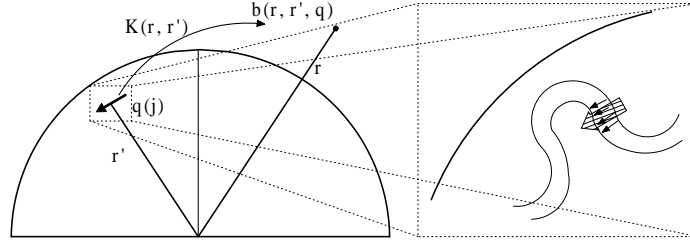
Figure 2.1: MEG forward model with spherical head model. (Left) When given an arbitrary source moment $\mathbf{q}$ locating at $\mathbf{r}'$ with orientation $\mathbf{j}$, it can derive the magnetic field at $\mathbf{r}$ outside the scalp by $\mathbf{b} = \mathbf{Kq}$. The head is modeled as the nested spheres with concentric, symmetric and homogenous property. (Right) It often exploits a equivalent current dipole (ECD) (big arrow) to represent a group of neighboring pyramidal neurons' electrical activities (tiny arrows) in the brain. These neurons locate at the cortex area with the orientation perpendicular to the cortical surface.

A MEG sensor is a coil to measure the magnetic flux through it. The measured magnetic flux is the integration of the partial component, parallel to the normal direction of the coil, of the magnetic field inside the circled area of the coil. Thus, the measurement of a sensor locates at $\mathbf{r}$ is

$$m(\mathbf{r}) = \int_A \mathbf{n} \cdot \sum_{\forall i} \mathbf{K}(\mathbf{r}, \mathbf{r}'_{\mathbf{i}}) \cdot \mathbf{q}_i \, d\mathbf{r}, \tag{2.18}$$

$$m(\mathbf{r}) = \sum_{\forall i} ((\mathbf{n} \cdot \int_A \mathbf{K}(\mathbf{r}, \mathbf{r}'_{\mathbf{i}}) \, d\mathbf{r}) \cdot \mathbf{q}_i), \tag{2.19}$$

where $\mathbf{n}$ and A are the the normal vector and the area circled by of the coil respectively. We can concatenate the equations for each sensor to represent the relationship of the dipole source and the recordings measured by all MEG sensors, that is,

$$\begin{pmatrix} m_1 \\ m_2 \\ \vdots \\ m_N \end{pmatrix} = \sum_{\forall i} \begin{pmatrix} (\mathbf{n}_1 \cdot \int_{A_1} \mathbf{K}(\mathbf{r}_1, \mathbf{r}'_{\mathbf{i}}) \, d\mathbf{r}_1) \cdot \mathbf{q}_i \\ (\mathbf{n}_2 \cdot \int_{A_2} \mathbf{K}(\mathbf{r}_2, \mathbf{r}'_{\mathbf{i}}) \, d\mathbf{r}_2) \cdot \mathbf{q}_i \\ \vdots \\ (\mathbf{n}_N \cdot \int_{A_N} \mathbf{K}(\mathbf{r}_N, \mathbf{r}'_{\mathbf{i}}) \, d\mathbf{r}_N) \cdot \mathbf{q}_i \end{pmatrix},$$

where N is the total number of the sensor. Because the parameters of the sensors is constant on the same MEG instrument, we can know these in advanced and can be omit they in the

equation. Therefore, we rearrange the equation to be

$$\mathbf{m} = \sum_{\forall i} \mathbf{G}(\mathbf{r'_i}) \cdot \mathbf{q}_i. \tag{2.20}$$

G is the gain matrix performing the transformation from a source to the MEG measurements. In practice, the integral part, for each sensor, in G can be approximated by the summation of the weighted magnetic fields at some discrete points inside the coil [49].

There are two issues about the forward model need to be concerned. First, it needs to be noted that the parameters of the positions and orientations of both sensors and source dipoles are all in the same coordinate system here, and so do they used in the following chapters. In practice, before the experiment, we need to derive the transformation from the coordinate system of head to that of MEG device and vice versa via the step of head position identification. Therefore, we can do the computation in either the spherical head or MEG device coordinate system. Second, we need to decide the center of the sphere, that is, the origin of the spherical head coordinate system. Usually, a good sphere center of the spherical head model can be determined by finding a sphere with most fit for the head geometry derived from MR image.

So far, when giving ECD sources in the brain, we can explicitly describes the measurement on all MEG sensors with an analytical formulation. Figure 2.2 gives an example of a forward solution when one dipole is or two dipoles are given. With the forward solution, we can utilize it for solving the inverse problem. Next chapter, we start to introduce a kind of the inverse algorithm and which is the most major part in this thesis, that is, beamforming methods.
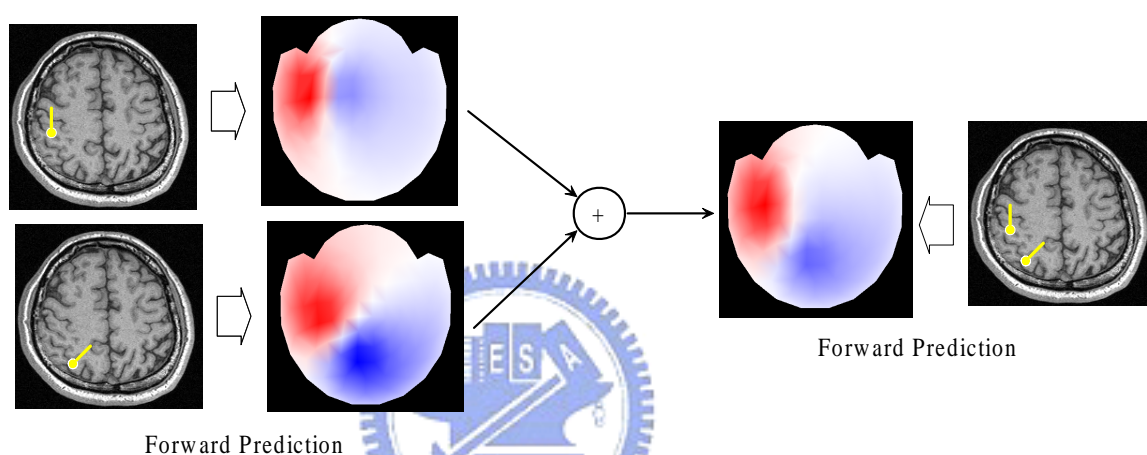
Figure 2.2: An example of the forward solution. We simulate the putative dipole(s) (yellow mark) in the head and then the resultant magnetic field recorded by sensors can be derives by the calculation of forward solution. If there are more than one source, the solution is the addition of the individual's. The magnetic filed topography is drawn by the interpolation of the sensors recordings estimated by Sarvas forward modal. The position of the sensors are unfolded to a plane for better visualization.

Chapter 3

Beamforming Methods for Functional Brain Imaging
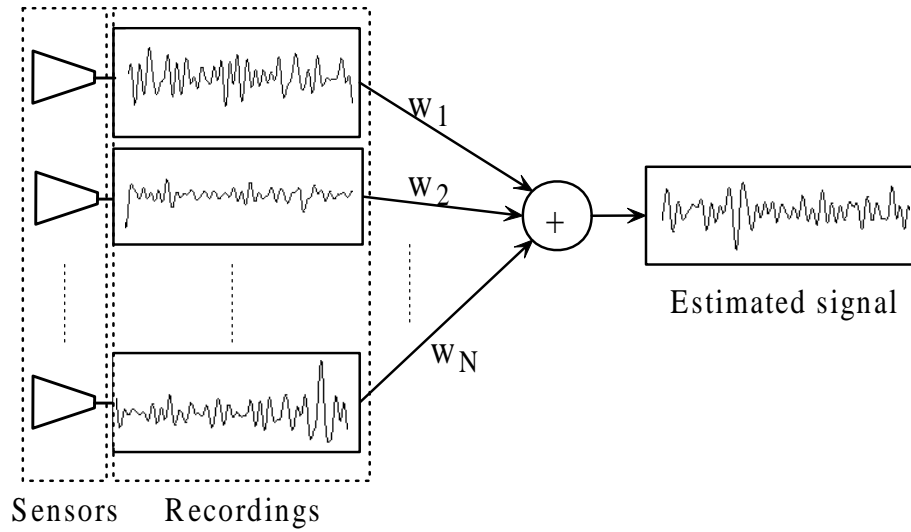
Figure 3.1: Basic concept of spatial filter. Spatial filter utilizes the recordings measured by sensors cites at distinct location to estimate the target source signal. It estimates the target source signal by summing the weighed recordings on each sensor. The kernel of the filter is the weighting coefficients designed by various criteria for different applications.

3.1 Introduction

Beamforming method [12, 33] is a well-known technique to localize the signal source in the array signal processing field and its developments can be traced from mid of twenty century. Today it is widely applied in sonar, radar, and astronomical telescope array systems. It is a spatial filter which weights different values, called beamforming coefficients, to each recording measured by each sensor at distinct cites. It then sums the weighted recordings as the estimated signal of the target source. Figure 3.1 illustrates the basic concept of spatial filter. We can think beamforming method utilizes the information recorded by physical sensors to create a virtual sensor at a specified position in the source space to measure the signals with a specified orientation. The kernel of the method is how to determine the beamforming coefficients, which is based on different assumptions in different algorithms for different applications.

The MEG inverse problem is a source localization problem with recordings measured by a set of sensors distributed outside the scalp. This is similar with the radar array system

and can be modeled as the problem solved by beamforming technique. Recently, algorithms [21, 54, 59, 72] based on this technique are developed to apply on solving MEG inverse problem and there are more and more MEG-related studies [7, 16, 25, 60, 62, 65, 68] exploit these methods for their applications which include the analyses of motor-, somatosensory- and auditory-related experiments. Figure 3.2 depicts that the beamformer applies to radar array system and to MEG inverse problem.

For detecting the brain source at a position with an orientation, the beamforming coefficients applying on each recordings of different MEG sensors is mainly determined by two criteria: retaining the targeted source exactly and, second, attenuating the effect cause by other sources. From the view of designing the filter, the spatially unit pass band of the filter is exactly at the specific position and orientation of the targeted source in one hand and, in the other hand, the filter tries its best to stop the contribution from other positions and orientations. These derives the filter with a unit gain constraint and minimum variance property. We will deduce the algorithm with much detail at the latter sections. By modifying the specified position and orientation, we can construct many virtual sensors distributing in the source space (brain) to image the electric activities in the brain.

Beside the beamforming method, other common methods that we briefly mentioned in Chapter 1 for solving MEG/EEG inverse problem includes least square dipole fitting, MNE and MUSIC. Least square dipole fitting method nonlinearly search the optimal dipole sources' parameters ,$\mathbf{r}'_i$ and $\mathbf{q}_i$ according to

$$min\|\mathbf{m} - \sum_{\forall i} \mathbf{G}(\mathbf{r}'_i) \cdot \mathbf{q}_i\|, \tag{3.1}$$

where $\mathbf{m}$ is the $N \times 1$ vector to represent the measured data on the N sensors at an instant time. This method does well and fast when the dipole number is small, but if the number is large, not only the computational cost of the nonlinear searching will dramatically increase but the objective function may much far from unimodal, that is, there will be many local minimum. Moreover, the major drawback of the method is that it need to determine the source dipole number in advance, which is unsuitable for real applications. The MNE method assumes that the sources are distributed currents. For deriving the source parameters, it minimizes not only the error between the real recordings and the estimated one, like least square dipole fitting, but the size (norm) of the distributed currents. The drawback
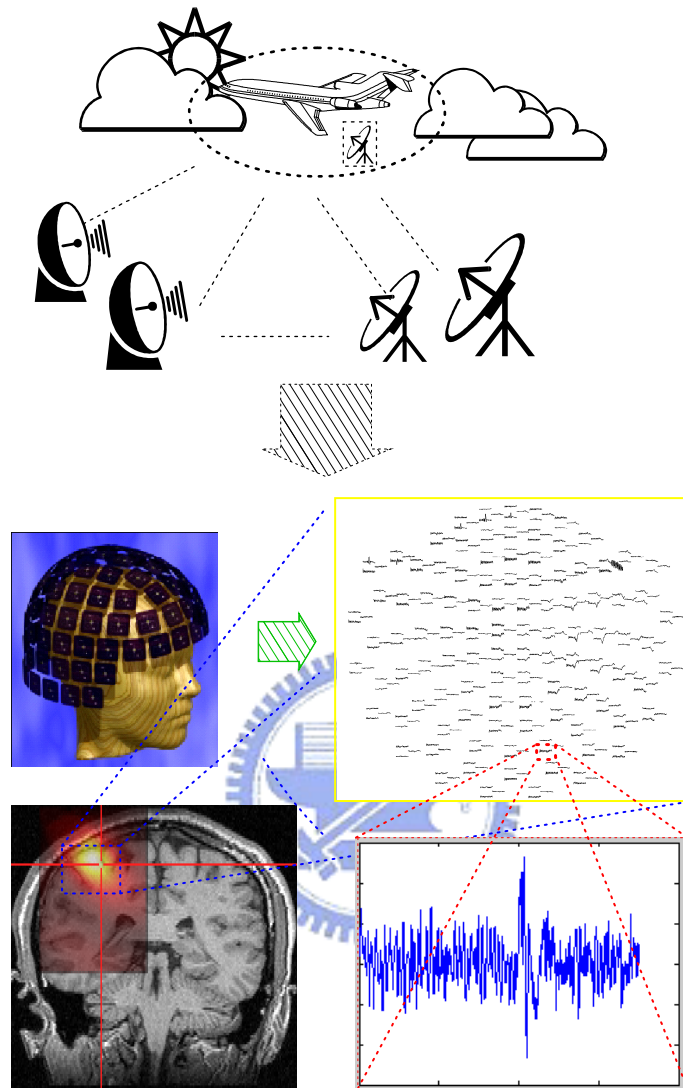
Figure 3.2: Example of the application of the beamforming technique: radar array system and MEG inverse problem. The upper figure shows that the radar array system uses the beamforming technique to put a virtue sensor (the small radar circled by the dash square) at a specify position in the source space (sky) for detecting if there is object (airplane) there. It can scan whole source space by shifting the virtue sensor. The same idea is adapted for solving the EEG/MEG inverse problem. That is, we put a virtue sensor (blue dash square) in the head to measure the signals at the specific position with the specific orientation and imaging the whole brain by moving the sensor through everywhere of the source space (brain). In both cases, the estimated signals (virtually measured by the virtual sensors) are constructed by summing the weighted recordings on physical sensors.

of the method is the solution will trend to the surface of the head because the effect of minimizing the norm of the source. MUSIC is a kind of spatial filter, which is designed by the criteria that will incline the estimated source orthogonal to the noise space which need to be estimated in advance.

Using beamforming method to solve MEG inverse problem has no need to know to the number of the sources in advanced and the resultant estimated sources have no tendency to the surface of the head which is suffered by MNE approach. Furthermore, unlike MUSIC, it has no need to estimate the noise space beforehand. Robinson and Vrba [55] also mentioned that the beamforming-based method is better than MUSIC for the study based on unaveraged MEG recordings. In this chapter, we start from the deduction of the basics of beamforming-based method to imaging the brain source significance at section 3.2.1 and 3.2.2. Next, we point out the difficulty about the determination of the source orientation for probe and the disadvantage of others' solution for it in the section 3.2.3. Consequently, at section 3.2.4, we propose a new method, maximum contrast beaformer, for solving the dilemma. After that, the DICS method which images the coherent sources is described at section 3.3.1 and 3.3.2 and its limitation. For solving it, we also proposed another new method, maximum normalized correlation beaformer, at section 3.3.3. Theoretically, the maximum normalized correlation beaformer can not only image the coherent sources in frequency domain but also in other domains if the auto- and cross-correlation are defined. We address the procedure of imaging the time-frequency coherent sources using proposed beamformer at the end of this chapter, section 3.3.4.

3.2   Source Estimation

3.2.1   Data Model

In time domain, bio-medical signal is often modeled as a random, or say chaotic, signal [5]. Random signal is the signal that we can not precisely predict its next features by its past history up to a significant level. The brain signal and the corresponding measured data by MEG are often modeled as the signal in this category. It needs to note that the model here is different with the source model mentioned in last chapter. They describe the temporal

and electromagnetical characteristics of the brain signals respectively.

In spatial domain, if the number of MEG sensors is N, the measured data can be view as a vector in a N dimension vector space that spanned by the basis of each sensor. The beamforming method solving MEG inverse problem spatially apples to the measured data of each sensor. That is, it performs a linear transform from the spatial domain and that is the reason why it is called "spatial" filter.

The unit-gain constraint and minimum variance beamformer uses the first and second order temporal statistic to feature both the measured data in the sensor-spanned space which equals the domain of the filter and the estimated source signal in the range of the filter. In the following, we first introduce the related notation for further deduction later.

First, involving the Sarvas forward model, if there are k dipoles in head, at a certain instance, the recordings $\mathbf{m}$ equals the summation of the productions of each gain matrix and its corresponding dipole moment:

$$\mathbf{m} = \sum_{i=1}^{k} \mathbf{G}(\mathbf{r}'_i)\, \mathbf{q}_i, \tag{3.2}$$

where $\mathbf{q}_i$ locating at $\mathbf{r}'_i$ is the dipole moment of the i-th in all k sources and $\mathbf{G}(\mathbf{r}'_i)$ is the corresponding gain matrix. Then, $\mathbf{m}$ is the summation of the effects by every source dipoles in the brain. Without of losing generality, we represent the source dipole in the Cartesian coordinate system such that $\mathbf{q}_i$ is a 3×1 vector and its elements represent x,y,z components of $\mathbf{q}_i$ respectively:

$$\mathbf{m} = \begin{pmatrix} m_1 \\ m_2 \\ \vdots \\ m_N \end{pmatrix}, \ \mathbf{q}_i = \begin{pmatrix} \mathbf{q}_{ix} \\ \mathbf{q}_{iy} \\ \mathbf{q}_{iz} \end{pmatrix},$$

and therefore, evidently, $\mathbf{G}(\mathbf{r}'_i)$ is a $N \times 3$ matrix. In real environment, it still needs to consider the noise so we add the noise $\mathbf{n}$ to the above equation such that

$$\mathbf{m} = \sum_{i=1}^{k} \mathbf{G}(\mathbf{r}'_i)\, \mathbf{q}_i + \mathbf{n}. \tag{3.3}$$

We then separate the dipole moment into orientation and magnitude parts, and combine the

former part and the gain matrix into ℓ, the lead field, that is,

$$\mathbf{m} = \sum_{i=1}^{k} \mathbf{G}(\mathbf{r}'_i) \, \mathbf{j}_i \, q_i + \mathbf{n} = \sum_{i=1}^{k} \ell(\theta_i) \, q_i \qquad (3.4)$$

where $\mathbf{j}_i = \mathbf{q}_i / \|\mathbf{q}_i\|$ is the orientation of the dipole source and we use θ to denotes both $\mathbf{r}'$ and $\mathbf{j}$. The subscript represents the number of the dipole as well.

Consequently, we consider the signals as a sequence of realization rather than just a value at an instant time, that is, we adds the temporal information into the notations. The above equation needn't modify, but the elements both in q_i and in $\mathbf{m}$ is no longer deterministic scalars but random variables which represent the random processes of the measured and source signals respectively. Then, we can define the first and second order statistics both of these two kind signals. It denotes mean and variance of the magnitude of a dipole as

$$\bar{q}_i = E\{q_i\} \qquad (3.5)$$

$$c_{q_i} = E\left\{ [q_i - \bar{q}_i][q_i - \bar{q}_i]^T \right\}, \qquad (3.6)$$

respectively [17], where E performs the expectation. Similarly, the mean and covariance matrix of the measured data are

$$\bar{\mathbf{m}} = E\{\mathbf{m}\} = \sum_{i=1}^{k} \ell(\mathbf{r}'_i) \, \bar{q}_i \qquad (3.7)$$

$$\mathbf{C} = E\left\{ [\mathbf{m} - \bar{\mathbf{m}}][\mathbf{m} - \bar{\mathbf{m}}]^T \right\} = \sum_{i=1}^{k} \left\{ \ell(\theta_i) \, c_{q_i} \, \ell^T(\theta_i) \right\} + \mathbf{C}_n , \qquad (3.8)$$

respectively, where $\mathbf{C}_n$ is the covariance of the noise under a usual assumption of zero mean.

In practice, it is online digitized for MEG recordings and which can be represented by a $N \times T$ matrix $\mathbf{M}$, where T is the sampling numbers. With out of generality, we assumes the weight of each sample point is identical. Hence, the covariance matrix of the recordings can be estimated by

$$\mathbf{C} = \frac{1}{N-1}\mathbf{M}_{MDF}\mathbf{M}_{MDF}^T, \qquad (3.9)$$

where $\mathbf{M}_{MDF}$ is the mean-deviation form [36] of $\mathbf{M}$, that is, every element in $\mathbf{M}_{MDF}$ is the corresponding element in $\mathbf{M}$ subtracting the arithmetic mean of the row at which the element lies.

3.2.2 Spatial Filter Design

As mentioned in section 3.1, the virtual sensor created by spatial filter is constructed by means of summing the weighted recordings of each sensors and this can be written as

$$y_0 = \mathbf{w}^T(\theta_0)\,\mathbf{m}, \tag{3.10}$$

where y_0 is the estimated scalar random signal at a specified position $\mathbf{r}'_0$ and with the orientation $\mathbf{j_0}$. $\mathbf{w}$ is the filter, the elements of which are the beamforming coefficients for weighting. The goal of the filter is that it can extract the targeted source with the parameter $\theta = \theta_0$ and suppress other non-targeted ($\theta \neq \theta_0$) interference. For achieving the goal, a unit-gain constraint and minimum variance spatial filter had be introduced, and its mathematical formula is

$$\min_{\mathbf{w}(\theta_0)} c_{y_0}\ \ s.t.\ \mathbf{w}^T(\theta_0)\,\ell(\theta_0) = 1 \tag{3.11}$$

where c_{y_0} is the variance of the estimated signal. The constraint in the formula performs the unit gain to targeted source for probe. It is because that if there is no noise and the forward model is exactly correct, then

$$y_0 = \mathbf{w}^T(\theta_0)\,\mathbf{m} = \mathbf{w}^T(\theta_0)\,\ell(\theta_0)\,q_0 = 1 \times q_0 = q_0, \tag{3.12}$$

where q_0 is the true source signal at the target position and orientation. The minimization operator tries its best to reduce the gain from other sources. The concept of unit-gain constraint and minimum variance is depicted in Figure 3.3. After substituting Eq. (3.8) into Eq. (3.11), we can get

$$\min_{\mathbf{w}(\theta_0)} \{\mathbf{w}^T(\theta_0)\mathbf{C}\mathbf{w}(\theta_0)\}\ \ s.t.\ \mathbf{w}^T(\theta_0)\,\ell(\theta_0) = 1 \tag{3.13}$$

The formulation is an equality-constrained optimization problem and can be solved by involving Langrange's theorem [8]. We omit the arguments of the functions for clarity and than the theorem tells that the optimal solution of Eq. (3.13) satisfies

$$\nabla(\mathbf{w}^T\mathbf{C}\mathbf{w}) + \lambda\nabla(\mathbf{w}^T\ell - 1) = 0 \tag{3.14}$$

$$(\mathbf{w}^T\ell - 1) = 0, \tag{3.15}$$
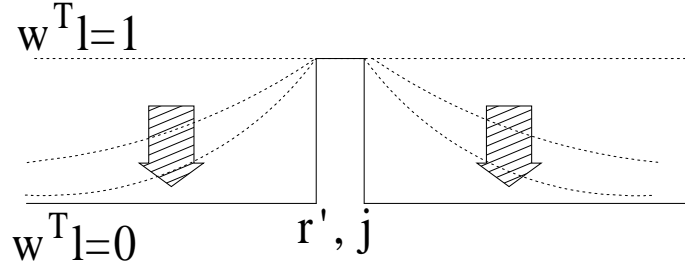
Figure 3.3: Spatial response of the unit-gain constraint and minimum variance spatial filter. For a specified position $\mathbf{r}'$ with orientation $\mathbf{j}$, the unit-gain and minimum variance spatial filter, first, is unit-gain at the position with the orientation and, second, tries its best to minimize the total gain from the source space. When the filter is ideal (real line), the gain is 1 ($\mathbf{w}^T \ell = 1$) exactly at $\mathbf{r}'$ with $\mathbf{j}$, otherwise it is 0 ($\mathbf{w}^T \ell = 1$).

where ∇ denotes the gradient operator and after it operates, Eq. (3.14) becomes

$$2\mathbf{w}^T \mathbf{C} + \lambda \ell^T = 0. \tag{3.16}$$

Rearranging and taking the transpose,

$$\mathbf{C}^T \mathbf{w} = \mathbf{C}\mathbf{w} = \frac{-1}{2}\lambda \ell. \tag{3.17}$$

The first equality in Eq. (3.17) is because of the symmetric property of covariance matrix. Next, multiplying $\mathbf{C}^{-1}$ on both sides of the last equality yields

$$\mathbf{w} = \frac{-1}{2}\lambda \mathbf{C}^{-1} \ell \tag{3.18}$$

Then, after multiplying ℓ^T on both sides of equal sign and according to the constraint in Eq. (3.13), we get

$$\ell^T \mathbf{w} = \frac{-1}{2}\lambda \, \ell^T \mathbf{C}^{-1} \ell = 1 \tag{3.19}$$

$$\lambda = -2 \, (\ell^T \mathbf{C}^{-1} \ell)^{-1} \tag{3.20}$$

Finally, substituting Eq. (3.20) into Eq. (3.18) derives the solution

$$\mathbf{w} = \mathbf{C}^{-1} \ell \, (\ell^T \mathbf{C}^{-1} \ell)^{-1} \tag{3.21}$$

This solution will try its best to approach to the ideal spatial filter with perfect spatial specificity for θ_0, that is, the gain is zero as $\theta \neq \theta_0$, otherwise it is 1. However, at this

time, the norm of the filter may be large such that it is very unstable and sensitive to the noise [72]. To comprise the spatial specificity and the noise sensitivity, a regularization tern is introduced to this optimizations problems [21, 54] and hence Eq. (3.13) and its corresponding solution becomes

$$\min_{\mathbf{w}(\theta_0)} \{\mathbf{w}^T(\theta_0)\mathbf{C}\mathbf{w}(\theta_0) + \alpha\mathbf{w}^T(\theta_0)\mathbf{w}(\theta_0)\} \ \ s.t. \ \mathbf{w}^T(\theta_0)\,\ell(\theta_0) = 1 \tag{3.22}$$

$$\mathbf{w} = (\mathbf{C} + \alpha\mathbf{I})^{-1}\ell\,(\ell^T(\mathbf{C} + \alpha\mathbf{I})^{-1}\ell\,)^{-1} \tag{3.23}$$

respectively, where α is the regularization parameter.

A statistical mapping of the neural activities are often used to find the source significance [54, 72]. The reason is that, first, the norm of the lead field is inversely-squared-proportional to the dipole depth, which is relative to the center of head model [58], such that the norm of the filter is intrinsically larger when the source is deeper, and so does the estimated source and that, second, both the distribution of the noise and the sensitivity of the sensors are not uniform spatially. Therefore, to obtain a meaningful statistical brain activation, F-statistic F is calculated as

$$F = \frac{\mathbf{w}^T\mathbf{C}_{act}\mathbf{w}}{\mathbf{w}^T\mathbf{C}_{ctr}\mathbf{w}}, \tag{3.24}$$

where $\mathbf{C}_{act}$ and $\mathbf{C}_{ctr}$ are the covariance matrices estimated by the samples from active and control states respectively. The active and the control states are the periods of the brain activities in which we are interested and we are not.

Here, we discuss the choice of $\mathbf{C}$, $\mathbf{C}_{act}$ and $\mathbf{C}_{ctr}$. It is no doubt that we can estimate $\mathbf{C}_{act}$ directly from the recordings in the period when the interesting brain activities cite. Oppositely, $\mathbf{C}_{ctr}$ can be estimated from the recordings in the period when the interesting brain activities do not cite or can exploit the empty room recordings for the estimation. If assuming the noise is uncorrelated, we can eliminate the elements in the non-diagonal part of $\mathbf{C}_{ctr}$. Moreover, If assuming the noise is independent identical distributed and the sensitivities of sensors are identical, we can use the identity matrix $\mathbf{I}$ as the control state covariance matrix. The period used to estimate $\mathbf{C}$ is the part to be suppressed its variance. If we set $\mathbf{C}$ the same with $\mathbf{C}_{act}$, the meaning is that the filter will suppress the contribution from $\theta \neq \theta_0$ according the statistic characteristic of the recordings in this period. Different

combination of $\mathbf{C}$, $\mathbf{C}_{act}$ and $\mathbf{C}_{ctr}$ gives different meaning of the results. However, by our experience and other literatures, except $\mathbf{C}_{act}$, we cannot concludes what is best for the choice of $\mathbf{C}$ and $\mathbf{C}_{ctr}$, that is, they still are options of the method.

Another parameter in the method, α, which perform the regularization between noise sensitivity and spatial specificity is difficult to be automatically determined because the value is dependent on the SNR. Actually, we always cannot compute the SNR in advance because we have no idea about the signal which just can be estimated after applying the inverse method. In practice, it often uses recordings to guide a rough rule for setting the value. By our experience and other literatures, we often set the value vary from 1 to 0.00001 times the maximum eigenvalue of $\mathbf{C}_{act}$. It needs to keep in mind that utilizing the maximum eigenvalue of $\mathbf{C}_{act}$ to derive an α is dominant by the maximum contribution of a certain source signal. That is, it is not able to concern the SNR of their sources, although there are no more proper ways yet.

3.2.3   Source Space Scanning Approaches

So far, when given a position $\mathbf{r}'$ and orientation $\mathbf{j}$, it can use the filter to estimate the source at the specified position and the specified orientation. Ideally, it should be applied at everywhere with every orientation for imaging the activities in whole brain. Nevertheless, infinitely computation is impossible, so sampling is adapted. It consequently encounters a problem: how much is the enough sampling rate? If we leave the computational ability and the limitation of the resolution caused by the number of MEG sensors aside, according to the Nyquest sampling theorem [50], the spatial sampling period of the position to apply the beamforming filter should be smaller than the half of the distance of the neighboring pyramidal neurons so that we can see the electrical activities of the individual pyramidal neurons. Although such extremely high sampling rate is almost impossible to be adapted when practice, this still tells us that sampling the space for the position to be probed for the filter is the finer, the better because the cortex area is tightly full of the neurons from microscopic view. However, it is not true for the issue of the orientation, because, at one position, the pyramidal neuron(s) from which the most measurements of MEG are contributed is (are) just (equivalently) one orientation, perpendicular to the cortical surface. In

the following, we discuss the issue about scanning the sources space by beamformer with the division of two categories, with and without the information of cortical surface geometry. Under each category, we discuss how it determines the position and orientation to be probed by beamformer respectively.

Some studies [29,41] utilize CT or MR image to construct the cortical surface geometry and solve the MEG inverse problem subject to the constraint that the source site at the position under the surface about $2mm$ with the orientation perpendicular to it. In practice, it often models the surface of a 3D object by triangle meshes, so does the cortical surface model. Continuously, they applied the beamforming filter in accordance with the position of and the normal vector of the vertices on the triangle meshes to do the sampling both for position and orientation, which is illustrated in Figure 3.4. Although this approach seems good for the reason that it fits the neurophysiology knowledge, an accurate enough cortical surface model is necessary [29]. However, segmentation, one of the most difficult task in image processing [19], of the convoluted cortical surface from the 3D volume image data is not trivial [18]. It usually needs a great effort to achieve an accurate enough surface model.

Without the cortical surface geometry, the other way simply samples the whole 3D space of the brain uniformly [21, 54, 59, 72] and there are different ways to determine the source orientation to probe in different studies. Van Veen et al. [72] applied the filter on three orthogonal axes, calculated the estimated source power on each axis and summed the results to be the final result as the source variance. They called the method linearly constrained minimum variance (LCMV) spatial filter and it was formulated as

$$\min_{\mathbf{W}(\mathbf{r}'_0)} \{trace(\mathbf{W}^T(\mathbf{r}'_0)\mathbf{C}\mathbf{W}(\mathbf{r}'_0))\} \; s.t., \; \mathbf{W}^T(\mathbf{r}'_0)\,\mathbf{G}(\mathbf{r}'_0) = \mathbf{I} \qquad (3.25)$$

where $\mathbf{W}$ is the a $N \times 3$ matrix with that each column represents the beamforming coefficients for each axis.

Probing the orientation solution space with few targeted direction like [72] is not proper because it is incorrect to think the source (fully) project to the axes. It has to sacrifice the spatial specificity by increasing the weight of regularization term α to avoid miss-detection, because the beamforming method does its best to suppress the signal other than the specified orientation. That is, when the filter approaches to ideal, we will find no contribution
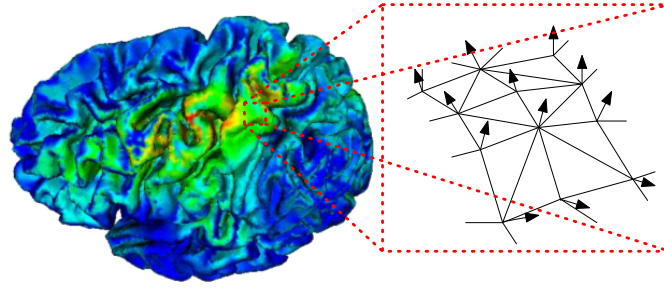
Figure 3.4: Determination of the position and orientation probed by beamformer when given the geometry model of the cortical surface. By the knowledge of neurophysiology, it is known that the electrical activities measured by MEG occur at cortical surface with the orientation perpendicular to it. After segmenting the cortical surface from the MR or CT image, it can construct and represent the cortical surface geometry by triangle meshes. Some studies apply the beamformer to the source space by sampling the position space at the position of the vertices on the mesh and, consequently, it determines the orientation as the vertex normal direction usually calculated by averaging the normal vectors of the connective triangle planes (right of the figure). The left of the figure is the resultant source power reconstructed by this approach for an finger lifting experiment [41]. The major difficulty of the approach is that accurately segmenting the convoluted cortical surface is not easy.

from a source except that it exactly lies on one of the sampling axes. Granted that the α is not approach to zero, the result image map is flatter than the one with correct source orientation because some parts of the contribution by the source are still lost due to the power annulation tendency of the filter. This predicament occurs as well in the approaches using cortical surface geometry model when the model is not accurate enough. By a simulation, Figure 3.5 gives an example of miss-detection when the targeted orientation of beamformer is far aberrant from the orientation of the true source.

Robinson and Vrba [54] proposed a method, "synthetic aperture magnetometery," (SAM). SAM searched the orientation on the plane tangential to the sphere of the head modal such that the value of z-deviate (performing the similar role to the F-statistic that mentioned in last section) is maximum, after sampled the orientation solution space. The method finds a meaningful orientation for probing and have no risk of missing the source if it indeed find the global maximum. Also, they [73] proved by deduction and showed by simulation that the result derived by SAM is more focal (opposite to flatter) than that derived by LCMV

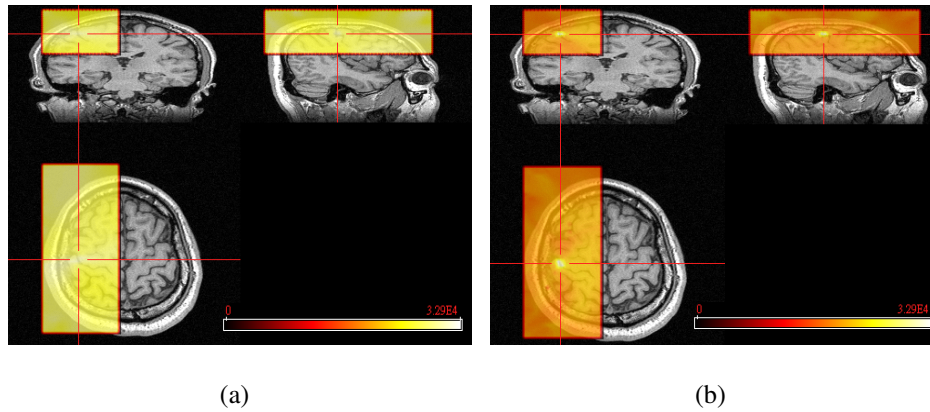(a)   (b)

Figure 3.5: Effect of miss-detection. We conduct a simulation experiment to demonstrate that there is the possibility of miss-detection when the targeted orientation is aberrant far from the orientation of the true source. We give a (target) source at the intersection of the red lines with an specific orientation and randomly assign noise sources in the head. We use (a) a specified wrong direction (which is aberrant from the ground truth 54 degree) and (b) maximum contrast beamformer to estimate the source power respectively. The results show that we can not find the difference between the area around position of the (target) source and other places when the targeted orientation is aberrant. Actually, the position with maximum value of the result differs form the ground truth in (a). Oppositely, we can clearly "see" the source by using maximum contrast beamformer which supposedly can find the targeted orientation approaching to the target source orientation. The color in the figure represent the comparative power which is normalized to $0 \sim 32767$ individually for each figure. It refers to later chapters for the maximum contrast beamformer and the simulation experiment.

around the neighboring location of the source, especially when SNR is high. The result was consistent with the aforementioned intuition by the essence of beamformer. However, the tradeoff is that the approach needs to spend more time for doing the search, especially the search is done exhaustively for the guarantee of finding out the global maximum. Figure 3.6 gives a short summary of the methods that the previous studies adapt to determine the position and orientation for probing without geometry information of the cortical surface.

(a) LCMV-based (in 3D space)
(b) SAM (in tangential plane)
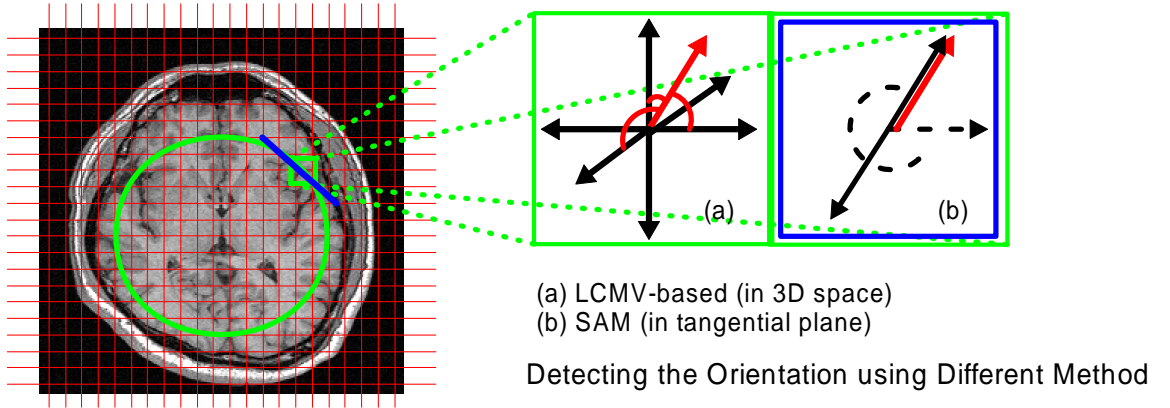
Detecting the Orientation using Different Method

Figure 3.6: Determination of the position and orientation probed by beamformer in general case. The left shows that it always samples the 3D space to determine the positions (intersection of the red line) for probing. The right shows that there are different ways to determine the orientation. Black arrows represents the targeted orientations (axes) and the red arrow is the true source orientation. (a) LCMV decomposed the orientation solution space with 3 orthogonal in 3D space. (b) SAM searches the orientation such that the resultant value of z-deviate is maximum.

3.2.4 Maximum Contrast Beamformer

In this section, we propose a new algorithm that can determine a proper orientation of the source for probing by beamformer. It has not only no probability of miss-detection of the source but less computational cost than exhaustive search. It is unit-gain constraint, minimum variance and maximum contrast beamforming method, hereafter calling it maximum contrast beaformer for short, for estimating the source. In the following, the algorithm will be elaborated.

We deduce the algorithm starting from taking apart the lead field ℓ in the solution of beamfoming method so that it becomes the multiplication of gain matrix $\mathbf{G}$ and target source orientation $\mathbf{j}$:

$$\mathbf{w} = \frac{(\mathbf{C} + \alpha\mathbf{I})^{-1}\ell}{\ell^T(\mathbf{C} + \alpha\mathbf{I})^{-1}\ell} = \frac{(\mathbf{C} + \alpha\mathbf{I})^{-1}\mathbf{Gj}}{\mathbf{j}^T\mathbf{G}^T(\mathbf{C} + \alpha\mathbf{I})^{-1}\mathbf{Gj}} \equiv \frac{\mathbf{Aj}}{\mathbf{j}^T\mathbf{Bj}}, \tag{3.26}$$

where $\mathbf{A}$ stands for $(\mathbf{C} + \alpha\mathbf{I})^{-1}\mathbf{G}$, B for $\mathbf{G}^T\mathbf{A}$ and we omit the arguments in each function for clarity. The step separates the targeted source orientation from the the current moment of source dipole such that no terms are dependent on $\mathbf{j}$ except $\mathbf{j}$ itself. Consequently, the

criterion to determine the optimal direction is maximum F-statistic (Eq. (3.24)), that is, the variance contrast of the control and active state is maximum:

$$\tilde{\mathbf{j}} = \arg\max_{\mathbf{j}} \frac{\mathbf{w}^T \mathbf{C_{act}} \mathbf{w}}{\mathbf{w}^T \mathbf{C_{ctr}} \mathbf{w}}. \tag{3.27}$$

Substituting Eq. (3.26) into Eq. (3.27),

$$\tilde{\mathbf{j}} = \arg\max_{\mathbf{j}} \frac{(\frac{\mathbf{Aj}}{\mathbf{j}^T\mathbf{Bj}})^T \mathbf{C_{act}} (\frac{\mathbf{Aj}}{\mathbf{j}^T\mathbf{Bj}})}{(\frac{\mathbf{Aj}}{\mathbf{j}^T\mathbf{Bj}})^T \mathbf{C_{ctr}} (\frac{\mathbf{Aj}}{\mathbf{j}^T\mathbf{Bj}})}. \tag{3.28}$$

The term $\mathbf{j}^T\mathbf{Bj}$ both in the numerator and denominator can be eliminated because it is a scalar, and then the expression becomes

$$\tilde{\mathbf{j}} = \arg\max_{\mathbf{j}} \frac{\mathbf{j}^T \mathbf{A}^T \mathbf{C_{act}} \mathbf{Aj}}{\mathbf{j}^T \mathbf{A}^T \mathbf{C_{ctr}} \mathbf{Aj}} = \arg\max_{\mathbf{j}} \frac{\mathbf{j}^T \mathbf{Pj}}{\mathbf{j}^T \mathbf{Q'j}} \cong \arg\max_{\mathbf{j}} \frac{\mathbf{j}^T \mathbf{Pj}}{\mathbf{j}^T \mathbf{Qj}}. \tag{3.29}$$

where $\mathbf{P} = \mathbf{A}^T \mathbf{C_{act}} \mathbf{A} \geq 0$, $\mathbf{Q'} = \mathbf{A}^T \mathbf{C_{ctr}} \mathbf{A} \geq 0$, and $\mathbf{Q} = (\mathbf{Q'} + \beta\mathbf{I}) > 0$. The symbol $\geq$ denotes that the all eigenvalues of the matrix are greater than or equal to zero. Similarly, the symbol $>$ denotes that the matrix is positive definite. $\beta\mathbf{I}$ performs regularization to guarantee that $\mathbf{Q}$ is of full rank. So far, because matrix $\mathbf{Q}$ is invertible and the scale of $\mathbf{j}$ is of nonsense to the result, the optimization problem can be solved by transform it to another optimization problem with an equality constraint [8] which is

$$\tilde{\mathbf{j}} = \arg\max_{\mathbf{j}} \mathbf{j}^T \mathbf{Pj} \quad s.t. \quad \mathbf{j}^T \mathbf{Qj} = 1. \tag{3.30}$$

Involving the Lagrangian theorem, the optimal solution must necessarily satisfies

$$\nabla(\mathbf{j}^T \mathbf{Pj}) - \lambda\nabla(\mathbf{j}^T \mathbf{Qj} - 1) = 0 \tag{3.31}$$

$$\mathbf{Pj} - \mathbf{Qj} = 0 \tag{3.32}$$

Pre-multiplying $\mathbf{P}^{-1}$ for each term of equation,

$$\mathbf{Q}^{-1}\mathbf{Pj} - \lambda\mathbf{Ij} = 0 \tag{3.33}$$

$$\mathbf{Q}^{-1}\mathbf{Pj} = \lambda\mathbf{j} \tag{3.34}$$

Hence, trivially, λ is the eigenvalue of the matrix $\mathbf{Q}^{-1}\mathbf{P}$ and the candidates for the solution is the corresponding eigenvectors. Continuously, we pre-multiply $\mathbf{j}^T\mathbf{Q}$ to both side of the equation, we have

$$\mathbf{j}^T \mathbf{Q}\mathbf{Q}^{-1}\mathbf{Pj} = \lambda\mathbf{j}^T \mathbf{Qj} \tag{3.35}$$

where $\mathbf{Q}\mathbf{Q}^{-1} = \mathbf{I}$ and $\mathbf{j}^T\mathbf{Q}\mathbf{j} = 1$, so
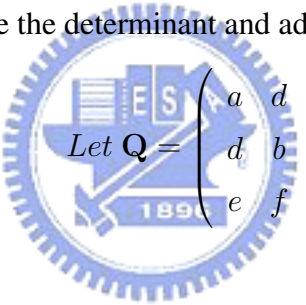
$$\mathbf{j}^T\mathbf{P}\mathbf{j} = \lambda \qquad (3.36)$$

That is, maximizing $\mathbf{j}^T\mathbf{P}\mathbf{j}$ equals maximizing λ, a eigenvalue of $\mathbf{Q}^{-1}\mathbf{P}$. Therfore, the solution $\tilde{\mathbf{j}}$ clearly is the eigenvector corresponding to the maximum eigenvalue of the matrix $\mathbf{Q}^{-1}\mathbf{P}$.

In practice, to calculate the inverse of a symmetric matrix and the maximum eigenvalue, eigenvector of an arbitrary square matrix can be solved iteratively by Jacobi's [52] and power method [6, 36] respectively; nevertheless, because these two matrix, $\mathbf{Q}$ and $\mathbf{Q}^{-1}\mathbf{P}$, are both 3×3, the closed-form solutions of the inverse and eigen problem exists. First, we can solve the inverse problem by the extension of the Cramer's rule [36],

$$\mathbf{Q}^{-1} = \frac{1}{\det(\mathbf{Q})} adj\mathbf{Q}, \qquad (3.37)$$

where $\det(\mathbf{Q})$ and $adj\mathbf{Q}$ are the determinant and adjugate of $\mathbf{Q}$ respectively. Hence,

$$Let\ \mathbf{Q} = \begin{pmatrix} a & d & e \\ d & b & f \\ e & f & c \end{pmatrix}.$$

The inverse of $\mathbf{Q}$ is

$$\mathbf{Q}^{-1} = \frac{1}{abc + 2edf - af^2 - be^2 - cd^2} \begin{pmatrix} bc - f^2 & ef - cd & df - be \\ ef - cd & ac - e^2 & de - af \\ df - be & de - af & ab - d^2 \end{pmatrix}.$$

Next, we solve the eigen problem of the matrix $\mathbf{Q}^{-1}\mathbf{P}$,

$$Let\ \mathbf{Q}^{-1}\mathbf{P} = \begin{pmatrix} a & b & c \\ d & e & f \\ g & h & i \end{pmatrix},$$

then the characteristic equation of which is

$$\det \begin{pmatrix} a - \lambda & b & c \\ d & e - \lambda & f \\ g & h & i - \lambda \end{pmatrix} = 0,$$

where λ is the eigenvalue to be solved. After expanding the equation, we have

$$\lambda^3 - (a+e+i)\lambda^2 - (-ae-ai-ei+eg+hf+bd)\lambda - (aei+bfg+cdh-cge-hfa-bdi) = 0.$$
(3.38)

For short, we let it be

$$\lambda^3 + \alpha_2\lambda^2 + \alpha_1\lambda + \alpha_0 = 0.$$
(3.39)

We can find the closed-form solution of the cubic equation by Cardan's formula [69] that

$$\lambda = k - \frac{1}{3\alpha_2},$$
(3.40)

$$k = w - \frac{p}{3w},$$
(3.41)

$$w^3 = \frac{q}{2} \pm \sqrt{\frac{q^2}{4} + \frac{p^3}{27}},$$
(3.42)

$$p = \frac{3\alpha_1 - \alpha_2^{\,2}}{3},$$
(3.43)

$$q = \frac{9\alpha_1\alpha_2 - 27\alpha_0 - 2\alpha_2^{\,3}}{27}.$$
(3.44)

The three paired cubic roots of w (w_1, w_2, and w_3) are

$$w_1 = \sqrt[6]{\Re^2(w^3) + \Im^2(w^3)}\,(\cos(\frac{\arctan(\frac{\Im(w^3)}{\Re(w^3)})}{3}) + \imath\sin(\frac{\arctan(\frac{\Im(w^3)}{\Re(w^3)})}{3}))$$
(3.45)

$$w_2 = w_1 \times \frac{-1 + \imath\sqrt{3}}{2}$$
(3.46)

$$w_3 = w_2 \times \frac{-1 + \imath\sqrt{3}}{2}$$
(3.47)

where $\Re(w^3)$ and $\Im(w^3)$ are the real and imagery parts of w^3 respectively, and $\imath$ equals $\sqrt{-1}$. Therefore, after solving the cubic roots of w, we will get three paired solutions and then back substitute into Eq. 3.40 to derive k and substitute k into Eq. 3.41 to get the three eigenvalues. It picks the maximum one, λ_{max}, and finds the kernel of the matrix $(\mathbf{Q}^{-1}\mathbf{P} - \lambda_{\mathbf{max}}\mathbf{I})$ by Gaussian elimination. Then, except $[0, 0, 0]^T$, the element in the kernel is exactly the eigenvector which corresponds to λ_{max} and this is what we want to obtain.

Else, we can find that there is some part in $\mathbf{P}$ and $\mathbf{Q}'$ can be computed off-line in advance, because

$$\mathbf{P} = \mathbf{A}^T \mathbf{C}_{act} \mathbf{A} = ((\mathbf{C} + \alpha \mathbf{I})^{-1} \mathbf{G})^T \mathbf{C}_{act} (\mathbf{C} + \alpha \mathbf{I})^{-1} \mathbf{G} \qquad (3.48)$$

$$\mathbf{P} = \mathbf{G}^T (\mathbf{C} + \alpha \mathbf{I})^{-T} \mathbf{C}_{act} (\mathbf{C} + \alpha \mathbf{I})^{-1} \mathbf{G}. \qquad (3.49)$$

It can find that $(\mathbf{C} + \alpha \mathbf{I})^{-T} \mathbf{C}_{act} (\mathbf{C} + \alpha \mathbf{I})$ is only dependent on the recordings and a pre-defined value α such that there is no need to recompute for every spatial sampling position when the filter scans the source space. The same processing is adapted for deriving $\mathbf{Q}'$. Estimating the covariance matrix is time-consuming because the high computational complexity of the matrix production [11], and here we show that our method still need to compute it once as LCMV and SAM.

The other issue of the method is about the choice of the value of β. The value of β is set according the precision of the floating-point number representation which is relative that a matrix is ill-posed or not due to the truncation error [6]. For instance, if we represent the numbers by IEEE floating-point format [45] with double precision, 11 bits for exponent part and 52 bits for mantissa, it can almost free from ill condition by setting the number β be greater than the minimum number in the diagonal elements of matrix $\mathbf{Q}'$ times $\frac{2^{-52}}{2}$. With out of losing generality, we can write the symmetric matrix $\mathbf{Q}'$ as

$$\mathbf{Q}' = \begin{pmatrix} a & c & d \\ c & b & f \\ d & f & c \end{pmatrix} = \begin{pmatrix} a_s + a_r & d_s + d_r & e_s + e_r \\ d_s + d_r & b_s + b_r & f_s + f_r \\ e_s + e_r & f_s + f_r & c_s + c_r \end{pmatrix},$$

where $a \geq b \geq c \geq 0$. The subscript s denotes the significant $\frac{2^{52}}{2}$ bits part and r denotes the residual part. The ill condition of Q occurs when

$$det \begin{pmatrix} a_s & c_s & d_s \\ c_s & b_s & f_s \\ d_s & f_s & c_s \end{pmatrix} = 0,$$

that is,

$$a_s b_s c_s + 2 d_s e_s f_s - b_s e_s{}^2 - a_s f_s{}^2 - c_s d_s{}^2 = 0$$

After adding the regulator $\beta\mathbf{I}$ with the aforementioned value of β and at the most strict condition that β is just significant to c, the determinant of $\mathbf{Q}'$ becomes

$$
\begin{aligned}
& a_s b_s (c_s + \beta_s) + 2 d_s e_s f_s - b_s e_s^{\,2} - a_s f_s^{\,2} - (c_s + \beta_s) d_s^{\,2} \\
= \; & (a_s b_s - d_s^{\,2})\beta_s + (a_s b_s c_s + 2 d_s e_s f_s - b_s e_s^{\,2} - a_s f_s^{\,2} - c_s d_s^{\,2}) \\
\equiv \; & \mathcal{A}\beta_s + \mathcal{B}
\end{aligned}
$$

where β_s is the significant part of β to c. Trivially, the determinant of $\mathbf{Q}$ will not be zero if when both $\beta_s \neq 0$ and $\beta_s \neq \frac{-\mathcal{B}}{\mathcal{A}}$. Therefore, we can say that $\mathbf{Q}$ will both be positive definite and almost free from the ill condition when we set $\beta_s > 0$, or we, for guarantee, can keep β_s away from falling into $\frac{-\mathcal{B}}{\mathcal{A}}$. In short, $\mathbf{Q}$ almost free from the ill-condition cause by the truncation error, if we set β be greater than the minimum number in the diagonal elements of matrix $\mathbf{Q}'$ times $\frac{2^{-\mathcal{P}}}{2}$, where $\mathcal{P}$ denotes the bit number for representing the mantissa part. If we want guarantee, we can still derive a rule from a deduction similar to the foregoing example. Although we can let $\mathbf{Q}$ free from the ill-condition by proper set the value of β, this regularization term changes the objective function in the optimal expression. At latter chapter, we will demostrate that a small but still sufficiently significant β will not only make $\mathbf{Q}$ free from singular but also make the solution almost retain origin by simulation.

In summary, we propose this maximum contrast beamforming method to determine the targeted source orientation to be probed according to a meaningful optimal criterion, maximum contrast, with no need of the time-consuming searching. The solution of this method is analytical and closed formed because all calculations consist only the basic arithmetic or matrix operations which can be done in deterministic steps. Besides, it needs to note that actually, the orientation is just can determined up to scale such that it is equivalent when the sign is positive or negative because the square operation in computing the variance. Hence, strictly speaking, it determines a axis rather than an orientation for probing the source and this is the same with LCMV and SAM.

3.3 Coherence Mapping

3.3.1 Signal Similarity

Before introducing the method to image the coherent sources, we make a description to the quantification of the similarity for two random signals. First, if two random signals are q_1 and q_2, and $\cdot$ denotes the inner product operation, the cross correlation is defined as

$$\phi(q_i, q_j) = E\{q_i \cdot q_j\} \tag{3.50}$$

which provides the information about how q_1 and q_2 vary jointly. Besides, if $i = j$ it calls $\phi(q_i, q_i)$ the autocorrelation of q_i. In additional, it defines that the cross density spectrum as

$$d_c(f, q_i, q_j) = H(f)\mathcal{F}\{\phi(q_i, q_j)\}, \tag{3.51}$$

to measure the signals similarity at a specific frequency band f when the Fourier transform exists. $\mathcal{F}$ denotes the Fourier transform and $H(f)$ is the ideal band pass filter with pass band f. However, it has a major shortcoming that it is dependent of the scale of q_1 and q_2. Hence, to eliminate the effect by the scale, it defines coherent as

$$d_c(f, q_i, q_j) = \frac{H(f)\mathcal{F}\{\phi(q_i, q_j)\}}{(H(f)\mathcal{F}\{\phi(q_i, q_i)\})(H(f)\mathcal{F}\{\phi(q_j, q_j)\})}. \tag{3.52}$$

Here, $d(f, q_i, q_i) = H(f)\mathcal{F}\{\phi(q_i, q_i)\}$ is called power density spectrum of q_i. Hence, the spectrum density matrix of of the recordings measured by MEG sensors is

$$\mathbf{D}(f) = H(f)\mathcal{F}\{\mathbf{C}\}, \tag{3.53}$$

In practice, a sampled signal with T sampling points can be use a $1 \times T$ vector $\mathbf{s}$ for representation. The autocorrelation of $\mathbf{s_i}$ and correlation, correlation coefficient of the signal $\mathbf{s_i}$ and $\mathbf{s_j}$ can usually be estimated as

$$\phi(\mathbf{s_i}) = \mathbf{s_i} \cdot \mathbf{s_i} \tag{3.54}$$

$$\phi(\mathbf{s_i}, \mathbf{s_j}) = \mathbf{s_i} \cdot \mathbf{s_j} \tag{3.55}$$

$$\rho(\mathbf{s_i}, \mathbf{s_j}) = \frac{(\mathbf{s_1} \cdot \mathbf{s_j})^2}{(\mathbf{s_i} \cdot \mathbf{s_i})(\mathbf{s_j} \cdot \mathbf{s_j})} \tag{3.56}$$

in order. Because the MEG signals that we deal with are online-digitized by the device, they have finite duration and finite amplitude, that is, the Fourier transform always exists for these data. It often uses the Welch's method [42] to estimate the spectral density. After overlapped segmenting original signals $\mathbf{s_i}$, $\mathbf{s_j}$ first and applying Hanning window to those segments, it calculates Fourier transformed vector $\mathbf{S}_i(f)$ and $\mathbf{S}_j(f)$ for a frequency band f. Each element in $\mathbf{S}_i(f)$ and $\mathbf{S}_j(f)$ is the contribution of each segment. For a specified band, it then respectively estimates the power spectral density, cross spectral density and coherence by

$$d(f, \mathbf{s_i}) = \mathbf{S_i}(f) \cdot \mathbf{S_i}(f) \tag{3.57}$$

$$d_c(f, \mathbf{s_i}, \mathbf{s_j}) = \mathbf{S_i}(f) \cdot \mathbf{S_j}(f) \tag{3.58}$$

$$Coh(f, \mathbf{s_i}, \mathbf{s_j}) = \frac{(\mathbf{S_i}(f) \cdot \mathbf{S_j}(f))^2}{(\mathbf{S_i}(f) \cdot \mathbf{S_i}(f))(\mathbf{S_j}(f) \cdot \mathbf{S_j}(f))} \tag{3.59}$$

3.3.2   DICS

A method, dynamic imaging of coherent sources (DICS) [22], and its consequent applications [23, 24] exploited the information of the brain electromagnetic signal in frequency domain to find out the coupling relationship between different activated regions in the brain for exploring the binding problem. As mentioned in Chapter 1 that almost studies for the problem analysis the recordings directly because there are comparative both late in development of and few in number of the inverse algorithms imaging the coherent sources. DICS is one of such method and is the only one based on the concept of beamforming. It has a similar process of the deduction with that of other beamforming methods introduced in the previous sections. DICS minimize the power spectrum of the estimated source which is in a narrow specified frequency band under the unit gain constraint, formulating as

$$\min_{\mathbf{w}(\theta_0)} \left\{ \mathbf{w}^T(\theta_0) \mathbf{D}(f) \mathbf{w}(\theta_0) + \alpha \mathbf{w}^T(\theta_0) \mathbf{w}(\theta_0) \right\} \ s.t. \ \mathbf{w}^T(\theta_0) \, \ell(\theta_0) = 1 \tag{3.60}$$

Similarly, the solution is

$$\mathbf{w} = (\mathbf{D}(f) + \alpha \mathbf{I})^{-1} \ell \left(\ell^T (\mathbf{D}(f) + \alpha \mathbf{I})^{-1} \ell \right)^{-1}. \tag{3.61}$$

By the way, for the utility in next section, we let

$$\mathbf{w} = \frac{\mathbf{A'j}}{\mathbf{j}^T \mathbf{B'j}}, \tag{3.62}$$

where $\mathbf{A}'$ stands for $(\mathbf{D} + \alpha\mathbf{I})^{-1}\mathbf{G}$, and $\mathbf{B}'$ for $\mathbf{G}^T\mathbf{A}'$.

Then, the power and cross density spectrum density between two sources are estimated by

$$d(f, q(\theta)) = \mathbf{w}^T(\theta)\mathbf{D}(f)\mathbf{w}^*(\theta), \tag{3.63}$$

$$d_c(f, q_1(\theta_1), q_2(\theta_2)) = \mathbf{w}^T(\theta_1)\mathbf{D}(f)\mathbf{w}^*(\theta_2), \tag{3.64}$$

respectively, where * denotes the complex conjugate. In this method, for reducing the computational complexity, the coherent is calculated between one reference signal defined in advance and other sources. Hence, reducing the above equation, the cross density spectrum density between the targeted source q_0 with θ_0 and the reference signal is

$$d_c'(f, q_0(\theta_0)) = \mathbf{w}^{\mathbf{T}}(\theta_0)\mathbf{d_c}(f, ref, \mathbf{m}), \tag{3.65}$$

where $\mathbf{d_c}(f, ref, \mathbf{m})$ is the cross spectrum density between the reference signal and the recordings on MEG sensors. This $N \times 1$ random vector can be estimated off-line in advance to reduce the cost of computation.

DICS applies the filter on the tangential plane to calculate the correlation between the target source and the reference signal and then find the principle axis on this 2D space spanned by the two direction as the source orientation. The resultant source orientation $\mathbf{j}_0$ is the optimal orientation that the cross density spectrum is maximum. Then, when given a position and an orientation, it calculates the coherence by

$$Coh(f, q_0(\theta_0), ref) = \frac{|d_c'(f, q_0(\theta_0))|^2}{d(f, q_0(\theta_0))\, d(f, ref)}, \tag{3.66}$$

where $d(f, ref)$ is the power density of the reference signal. After scanning the whole brain, it can construct a image for representing the coherent level of the signal at each place with the reference signal.

DICS can just imaging the coherent sources in a fixed narrow frequency band along with time because the estimation of the cross density spectrum density matrix of the recordings is under the assumption that the signal is stationary, the frequency statistic characteristics of the random signal is independent with time. The assumption is not the general case for the brain signals which reveals in some studies, for instance, Pfuirtscheller [51] found that the brain signal will behave as desynchronization or synchronization in some cases like

movement and memory. Bressler [4] also revealed that the coherence occurs at multiple frequency band by the monkey study.

3.3.3   Maximum Normalized Correlation Beamformer

The beamforming-based algorithm can be used for imaging the source power and the coherent sources. At previous section, we developed the maximum contrast beamforming method to determine the target source orientation for imaging the source power. Here, in this section, we will propose the unit gain constraint, minimum variance and maximum normalized correlation beamforming method, similarly calling it maximum normalized correlation beamformer for short. It also determines a meaningful orientation of targeted source for theoretically not only imaging the coherent sources in the frequency domain with a narrow band like DICS but also imaging the the sources with high normalized correlation in the domain where the auto- and cross-correlation is defined. Besides, the method is under a prerequisite that a reference signal for calculating the relation to other sources is given in advance, like DICS. Following, we deduce the method with constraint in the maximum coherent condition first for easy comprehension.

The goal of the method is that we want to determine a source orientation such that the coherent between the estimated signal and a specified reference signal is maximum, that is

$$\tilde{\mathbf{j}}_0 = \arg \max_{\mathbf{j}_0} Coh(f, q_0(\theta_0), ref) = \frac{|d'_c(f, q_0(\theta_0))|^2}{d(f, q_0(\theta_0))\, d(f, ref)}. \tag{3.67}$$

Because the reference signal is determined, we can normalize it off-line in advance such that $d(f, \hat{ref}) = 1$, where $\hat{ref}$ denotes the normalized reference signal. Consequently, we abbreviate the arguments of the function and then substitute Eq. 3.63 and Eq. 3.65 into Eq. 3.67 such that

$$\tilde{\mathbf{j}}_0 = \arg \max_{\mathbf{j}_0} \frac{|\mathbf{w^T d_c}|^2}{\mathbf{w}^T \mathbf{D} \mathbf{w}^*}, \tag{3.68}$$

$$\tilde{\mathbf{j}}_0 = \arg \max_{\mathbf{j}_0} \frac{\mathbf{w}^T \mathbf{d_c} \mathbf{d_c}^{*T} \mathbf{w}^*}{\mathbf{w}^T \mathbf{D} \mathbf{w}^*}, \tag{3.69}$$

$$\tilde{\mathbf{j}}_0 \equiv \arg \max_{\mathbf{j}_0} \frac{\mathbf{w}^T \mathbf{D_c} \mathbf{w}^*}{\mathbf{w}^T \mathbf{D} \mathbf{w}^*}, \tag{3.70}$$

where $\mathbf{D_c}$ is the $N \times N$ cross spectrum density matrix between the recordings on each sensor and a specified reference signal. Then replacing $\mathbf{w}_\theta$ by Eq. (3.63),

$$\tilde{\mathbf{j}}_0 \equiv \arg\max_{\mathbf{j}_0} \frac{(\frac{\mathbf{A}'\mathbf{j}}{\mathbf{j}^T\mathbf{B}'\mathbf{j}})^T \mathbf{D_c}(\frac{\mathbf{A}'\mathbf{j}}{\mathbf{j}^T\mathbf{B}'\mathbf{j}})^*}{(\frac{\mathbf{A}'\mathbf{j}}{\mathbf{j}^T\mathbf{B}'\mathbf{j}})^T \mathbf{D}(\frac{\mathbf{A}'\mathbf{j}}{\mathbf{j}^T\mathbf{B}'\mathbf{j}})^*}, \tag{3.71}$$

So far, we find that it is similar with the deduction of maximum contrast beamformer, hence

$$\tilde{\mathbf{j}} = \arg\max_{\mathbf{j}} \frac{\mathbf{j}^{*T}\boldsymbol{\Gamma}\mathbf{j}}{\mathbf{j}^T\boldsymbol{\Upsilon}'\mathbf{j}^*} \cong \arg\max_{\mathbf{j}} \frac{\mathbf{j}^T\boldsymbol{\Gamma}\mathbf{j}^*}{\mathbf{j}^T\boldsymbol{\Upsilon}\mathbf{j}^*} \tag{3.72}$$

where $\boldsymbol{\Gamma}$ stands for $\mathbf{A}'^T\mathbf{D_c}\mathbf{A}'$ and $\boldsymbol{\Upsilon}'$ for $\mathbf{A}'^T\mathbf{D}\mathbf{A}'$. $\boldsymbol{\Upsilon} = \boldsymbol{\Upsilon}' + \beta\mathbf{I}$ results from the same reason discussed in the derivation of maximum contrast beamformer. Hence the optimal targeted orientation is the eigenvector of $\boldsymbol{\Upsilon}^{-1}\boldsymbol{\Gamma}$ corresponding the maximum eigenvalue. In fact, it has no need to explicitly compute the eigenvector and back substitute to compute the lead field for deriving the filter $\mathbf{w}$, if we just want to visualize the value of the coherence. it is because of, by referring and Eq. 3.36 and the constraint in Eq. 3.30, that the maximum eigenvalue is exactly the same with the maximum coherence. Otherwise, we can substitute the solution into Eq. 3.62 for other utilization.

By substituting the cross- and auto-spectrum density matrix with a predefined cross- and an auto-correlation matrix of recordings and a normalized reference signal representant in a certain domain, we can image the normalized correlation level between the sources and the reference signal in that domain. Other properties of this method is very similar with the maximum contrast beamformer, that it still can analytically compute the result in deterministic steps with a meaningful targeted orientation and the cross- and auto-correlation matrices just be estimated only once in advance.

3.3.4   Time-frequency Coherent Sources Mapping

As mentioned previously, the limitation of DICS is that it needs to assume the brain signal is stationary and constrained in a narrow frequency band because it is based on Fourier analysis. In this section, we will develop a procedure which applies the maximum normalized beamformer to imaging the time-frequency coherent sources without the limitation as DICS by using the Morlet wavelet to transform an estimated brain source signal and a reference signal to time-frequency domain before compute the coherence of the selected wavelet coefficients of these two signals as the measurement of their coherent level. Here

we constrain that the coherent in time-frequency domain is event-related, like [14, 53, 66], that is, the source signal has the same statistical characteristics at a certain time-frequency point cross every tasks performed in the same way. At this condition, it usually repeats the same task several times, called one trial for one time, to obtain sufficient statistics for further processing. In short, this proposed procedure images the coherent sources in both time-frequency domain and in the cortex level by using beamforming-based inverse technique.

Here we choose the wavelet analysis to represent the signals such that majorally it can free from the limitation of the Fourier analysis, i.e. the signal must be stationary. Although short-time Fourier analysis is also with the ability, wavelet is still more flexible and more suitable than it for locally analyzing signals because the targeted window could be variable to a proper size but the window of short-time Fourier analysis is fixed. The details of the wavelet, short-time Fourier analysis, and their comparisons are beyond the scope of the thesis and that can be find in [10, 50] for short-time Fourier, and [9, 28] for wavelet and the comparisons. Consequently, the complex Morlet wavelet [67] is adapted by us to describe the the signal in both time and frequency domain. The kernel of the Morlet wavelet is the kernel of the Fourier transform windowing by a Gaussian filter. Due to the the property of the kernel, it can indicate the "frequency" rather than just the "scale" like other wavelet kernels. This ability results that it are often exploited to apply on the brain signals for the studies of the binding problem [23, 39, 40, 57, 67].

In practice, we start our procedure from applying the Morlet wavelet transform (MWT) to the specified reference signal and the recordings, that is

$$\mathbf{v}_{ref} = \varphi\{\mathbf{s}_{ref}^T\} \tag{3.73}$$

$$\mathbf{V}_M = \varphi\{\mathbf{M}^T\}, \tag{3.74}$$

where $\mathbf{v}_{ref}$ is $(T_{mwt} \times F_{mwt}) \times 1$ vector consisting the Morlet wavelet coefficients of the reference signal within an interesting time period with T_{mwt} sampling points and cross an interesting frequent band with F_{mwt} sampling points. Figure 3.7(a) gives an example. The symbol $\varphi\{\cdot\}$ denotes the Morlet wavelet transform. $\varphi\{\mathbf{M}^T\}$ represents that it do the transform for each row of M and hence $\mathbf{V_M}$ is a $(T_{mwt} \times F_{mwt}) \times N$ matrix that each row represents the Morlet wavelet coefficients of the realization (recordings) on each sensor.
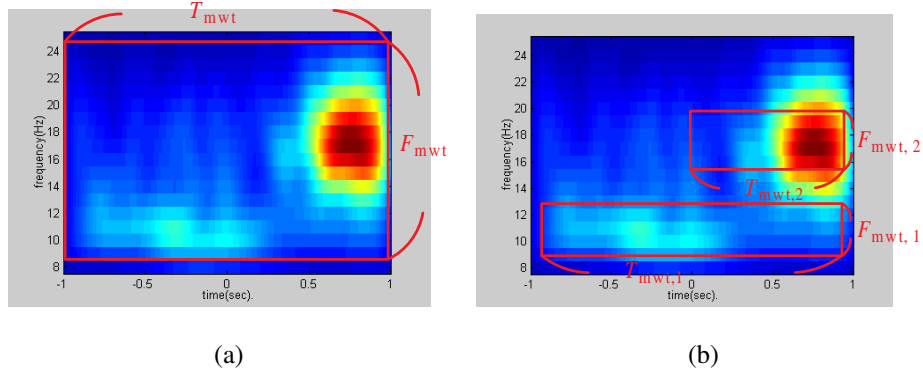
(a)   (b)

Figure 3.7: Examples of choosing the interesting region on time-frequency map. Both The figures are the time-frequcny map of a given signal and we can select the interesting region for computing the correlation coefficient cross the selected wavelet coefficients. (a) A connective $T_{mwt} \times F_{mwt}$ rectangular window. (b) Two disconnected windows for different region of interesting (ROI) on time-frequency map. It notes that the figures here is the time-frequency power map for simplifying the demonstration. Actually, we select the ROI on the time-frequency map consisting with the complex wavelet coefficients.

Continuously, for one trial, the auto-correlation matrix $\mathbf{D}_{mwt,i}$ of the recordings in this wavelet domain can be computed as

$$\mathbf{D}_{mwt,i} = \mathbf{V}_{\mathbf{M}_i}^T \mathbf{V}_{\mathbf{M}_i}^*. \tag{3.75}$$

The square of the cross-correlation matrix $\mathbf{D}_{c,i,mwt}$ between the recordings and reference signal in the wavelet domain is

$$\mathbf{D}_{c,mwt,i} = \mathbf{V}_{\mathbf{M}_i}^T \mathbf{v}_{\mathbf{ref}}^* \mathbf{v}_{\mathbf{ref}}^{\mathbf{T}} \mathbf{V}_{\mathbf{M}_i}^*. \tag{3.76}$$

For the event-related time-frequency coherence, we estimate the autocorrelation and cross-correlation matrices, $\mathbf{D}_{mwt}$ and $\mathbf{D}_{c,mwt}$ by

$$\mathbf{D}_{mwt} = \frac{1}{N} \sum_{\forall i} \mathbf{D}_{mwt,i}, \tag{3.77}$$

$$\mathbf{D}_{c,mwt} = \frac{1}{N} \sum_{\forall i} \mathbf{D}_{c,mwt,i}, \tag{3.78}$$

respectively. Then, we can substitute $\mathbf{D}_{mwt}$ and $\mathbf{D}_{c,mwt}$ into the maximum normalized correlation beamforer to image the coherent level in the time-frequency domain between the signals in the brain and the specified reference signal.

Actually, we can arbitrarily choose the interesting wavelet coefficients on the time-frequency map. Figure 3.7 (b) gives an instance that we can choose the coefficients discontinuously such that at this example, the dimension of $\mathbf{v}_{ref}$ is $(T_{mwt,1} \times F_{mwt,1} + T_{mwt,2} \times F_{mwt,2}) \times 1$ and, similarly, $\mathbf{V_M}$ is a $(T_{mwt,1} \times F_{mwt,1} + T_{mwt,2} \times F_{mwt,2}) \times N$ matrix. If we just select the region of interesting (ROI) on the time-frequency map as a narrow band like the lower red rectangle in Figure 3.7 (b), the condition is similar with DICS.

Finally, we conclude the procedure of imaging the (event-related) time-frequency coherence. First we transform the reference signal $\mathbf{s}_{ref}$ from time course representation to the time-frequency representation by Morlet wavelet coefficients among which we select the interesting coefficients. The same step applies to the recordings for every trial, $\mathbf{M}_1$, $\mathbf{M}_2$, ..., $\mathbf{M}_k$, if we have k trials. So far, we can compute the $\mathbf{D}_{mwt,i}$ and $\mathbf{D}_{c,mwt,i}$ for each trial using the selected coefficients both of $\mathbf{s}_{ref}$ and $\mathbf{M}_i$. After that, the auto- and cross-correlation matrix, $\mathbf{D}_{mwt}$ and $\mathbf{D}_{c,mwt}$, can be estimated by averaging all $\mathbf{D}_{mwt,i}$ and $\mathbf{D}_{c,mwt,i}$ respectively. Then we can substitute these two matrixes into the proposed maximum normalized correlation beafomer to imaging the coherent level of each estimated brain signal with the reference signal in the domain of the interested (selected) region(s) in the time-frequency domain. Figure 3.8 illustrates the procedure.
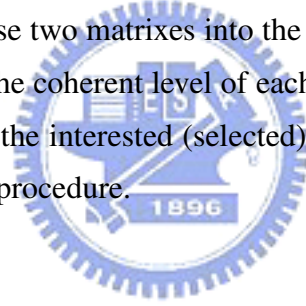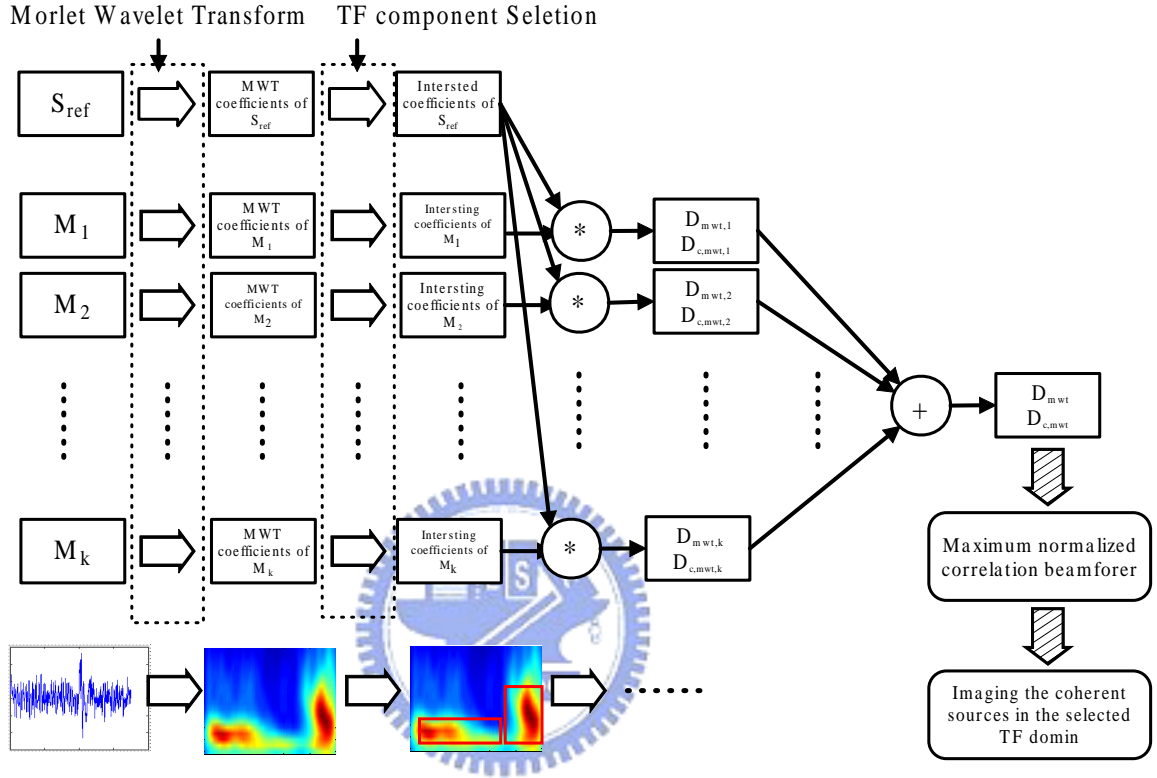
Figure 3.8: Procedure of imaging (event-related) time-frequency coherence. First we transform the reference signal s_{ref} from time course representation to the time-frequency representation by Morlet wavelet coefficients among which we select the interesting coefficients. The same step applies to the recordings for every trial, M_1, M_2, ..., M_k, if we have k trials. So far, we can compute the $D_{mwt,i}$ and $D_{c,mwt,i}$ for each trial using the selected coefficients both of s_{ref} and M_i. After that, the auto- and cross-correlation matrix, D_{mwt} and $D_{c,mwt}$, can be estimated by averaging all $D_{mwt,i}$ and $D_{c,mwt,i}$ respectively. Then we can substitute these two matrixes into the proposed maximum normalized correlation beafomer to imaging the coherent level of each estimated brain signal and the reference signal in the domain of the interested (selected) region(s) in the time-frequency domain

Chapter 4

Experiment Results

For demonstration and verification, we implement the procedures for processing the MEG data from raw recordings to, finally, the brain activities estimated by proposed inverse algorithms. The procedures are implemented in C/C++ language, compiled by Microsoft Visual C++ 6.0 compiler and executable on MS-Win32 platform. All floating-point calculations follow the IEEE floating-point format with double precision. Sarvas forward model is adapted for all inverse algorithms that we implement. The recordings are derived from simulation, phantom and real experiments. In phantom and real experiments, the recordings are recorded with a whole-head neuromagnetometer (Vectorview, Neuromag Ltd., Finland) comprising two orthogonal planar gradiometers at 102 distinct locations. The phantom supplied by the manufactory as the MEG instructions. In simulation, computer generates putative sources and then compute the estimated recordings on the aforementioned 204 sensors according to the given forward model. In the following, we first introduce the pre-processing that enhance signal to noise ratio before the further processing. Next, we will use the simulation and phantom experiments to verifying the proposed algorithms. Finally, we apply our method to the recordings from finger lifting experiments.

Data Preprocessing

As we mentioned in Chapter 1, the brain signal is comparatively small than the confounding and environmental noise. For the sake of enhancing the SNR, preprocessing for the recordings is necessary before the further processing. At first, it needs to keep in mind that due to the brain signal is usually modeled by random signals such that EEG or MEG experiment usually repeats the same task several times, called one trial for one time, to obtain sufficient statistic. Consequently, we briefly introduce the usual preprocessing steps for MEG recordings. First, the significant action of the body or the eye blinking cause large currents which greatly influence the measurements. Hence, by finding out the unusual scale recordings both on MEG sensors and on electric ocular graph (EOG) channels that measure the electric potential around the eyes, surge and EOG rejection drop or compensate the trials that are stained by those artifacts. Second, signal space projection (SSP) [70] is often exploited to eliminate the unbalanced noise effect on different sensors. SSP projects the recordings to the space which is orthogonal to the noise space estimated by empty room
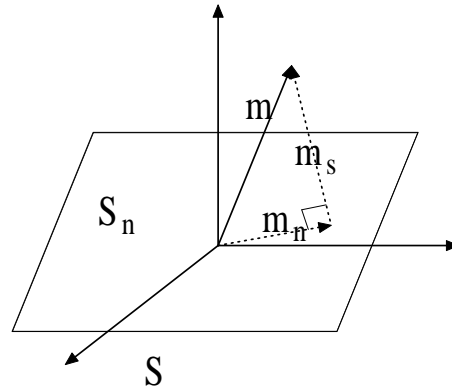
Figure 4.1: Concept of signal space projection (SSP). To spatially eliminate the noise, SSP projects the original recordings $\mathbf{m}$ in the space S to a signal space that is orthogonal to the noise space S_n, that is, it eliminates the contribution from the noise component m_n. The space S is spatially spanned by the basis of the sensors, that is, the dimension of it is the same with the number of the sensor. Noise space S_n is a subspace of S and is spanned by the leading principle components estimated from empty room recordings which are all assumed noise. For simplicity, the figure just depicts the concept within 3D and could expand to any dimension.
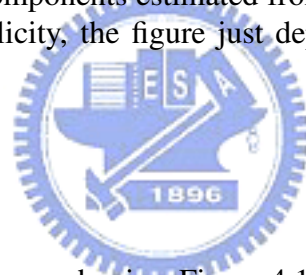
recordings which are all assumed noise. Figure 4.1 shows the concept of SSP. Temporally, because breath, heartbeat are about 1 time per second and the power line consists alternating current with 60Hz and its harmonic, band pass filter is used to filter out these interferences. Moreover, the recordings on each sensors may drift along with time, so baseline correction drags the recordings by subtracting a baseline that, for each trial, usually is estimated by the mean of the recordings in the control state period which is supposedly the period with no interesting activation in the brain. Besides, if the interesting activation is a time-locked and phase-locked signal respecting to the stimuli, that is, such brain signal appears not only with an approximately fixed time but with approximately same shape after the stimuli on-set cross each trial, we can align the trails by the (stimulus) onset time and synchronously average the trials. According to well-known central limit theorem, this can eliminate the variance of the recordings contributed by the random noise proportional to the number of the trials. Summarily, the integrated preprocessing flow is illustrated in Figure 4.2.
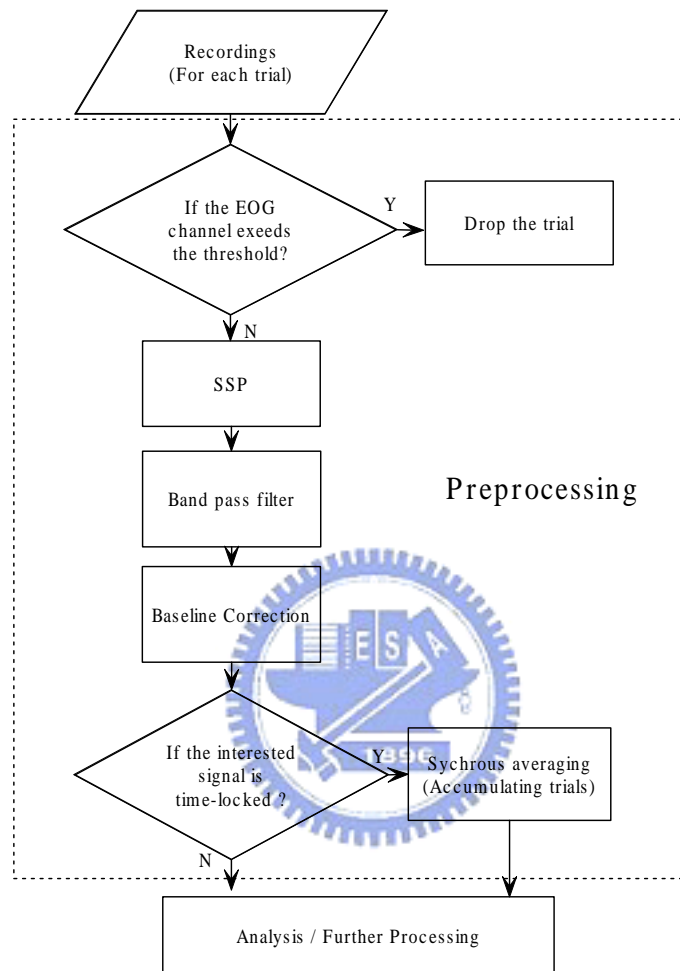
Figure 4.2: Usual preprocessing for MEG recordings. For enhancing the SNR for the MEG recordings, preprocessing is needed before the further analysis or futher processing. The EOG rejection drops the trial when corresponding EOG recordings exceed a specified threshold. SSP projects the recordings to the signal space to flat the spatially disproportionate noise distribution. Band pass filter temporally filters out the interference by power line and some physiological phenomenon like breath or heartbeat. The baseline correction overcomes the drift effect of the signals often caused by hardware or background environments. If the interested brain phenomenon is time-locked and phase-locked to the stimuli, it can average all trials to eliminate the contribution by random noise.

4.1 Simulation and Phantom Experiment

We conduct simulation and phantom experiment which have the ground truth of the parameters of the (putative) sources for verifying and demonstrating the proposed algorithms, maximum contrast and maximum normalized correlation beamformer. Simulating experiment is the one that we can control any condition and have the ground truth. We always not only know but easily modify every parameter of every component in the experiment. We simulate the recordings by the forward model adding some noise when it gives a dipole or dipoles in advance. The noise is assigned by two manners, noise sources and sensor noise. The noise sources are the random sources with the amplitudes following the Gaussian distribution temporally and uniformly distributed in- or out-side a putative sphere head spatially. The senor noise is the zero mean Gaussian random process and the noise is added directly to the recordings. The standard deviation of the sensor noise is determined according to the real empty room measurements. After applying the inverse algorithm, we can compare the estimated source with the true parameters of the dipole that we gives. The dominant drawback of the method is that it is very difficult to simulate all effects caused by real brain and environment. Although the absolute sampling rate is nonsense in the simulation, in the following, we use 1 kilo-Hz as the sampling frequency for easy description. Another, the phantom is a hardware device with a semi-sphere shape in which some circuits are cited to simulate the occurrence of current dipole in the brain. The configuration of phantom device is illustrated in Figure 4.3. The phantom experiment was conducted by electrifying a selected circuit loop and measured the recordings by MEG sensors after sitting the "phantom" into the MEG device. It provides a condition that is more approximate to real experiment then the simulation and with the ground truth of the sources as well. However, we can not arbitrarily modify the parameters of the sources because which are limited by the configuration of the hardware intrinsically.

4.1.1 Forward Model Accuracy

In Chapter 2 we describes the MEG Sarvas forward model which has an analytical solution and an acceptable accurate simultaneously. Here, we adapt least square dipole
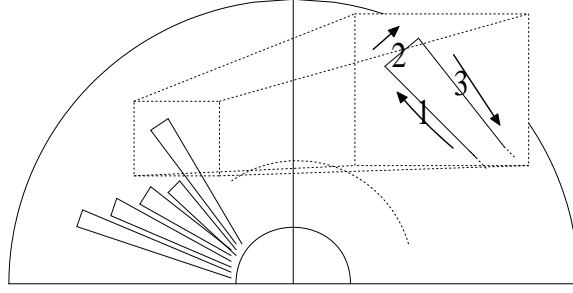
Figure 4.3: Configuration of phantom. Phantom is a hardware device with a semi-sphere shape in which some circuits are cited to simulate the occurrence of current dipole in the brain. When we electrifying a selected circuit loop, the current flow through the circuit line like the magnifying figure on right. Segments 1 and 3 can be supposed parallel to each other, because they are relative longer than segment 2. Hence the induced magnetic field contributed by the current on segment 1 and 2 can be considered counteraction. It then can equip the circuit to a dipole locates at the mid point of segment 2 with the moment specified by both the amplitude of the current and the length of segment 2.

fitting method and the phantom experiment recordings to re-verify the accuracy of the model. The phantom source is a 16.67 Hz sine wave with the amplitude of 50nAm. We use band pass filter to filter out the signal other than $7.5 \sim 35$ Hz and than average 50 trials. Dipole fitting algorithm fits the dipole according to the recordings at the peak five point of the sine wave. The results are shown in Figure 4.4 that the average localization error is about $1mm$ which is no great difference with the prior studies [34, 37, 44].

4.1.2 Regularization Term β

In the equation Eq. 3.29 and Eq. 3.72, we add the regularization term $\beta\mathbf{I}$ to $\mathbf{Q}$ and $\mathbf{\Upsilon}$ to prevent the ill-condition for computing matrix inverse. However, it changes the result of the optimization expression to influence the resultant orientation of the target source. Here, we demonstrate the effect of the regularization term. The simulated source is a pure sine wave with amplitude 50nAm, locates at the sensorimotor area of the putative head (source1 in Figure 4.5). It follows the uniform distribution to randomly assign the source orientation resisted on the tangential plane to the sphere of the head model. For focusing on the effect of the term, we set signal to noise ratio (SNR) high that the noise sources are zero
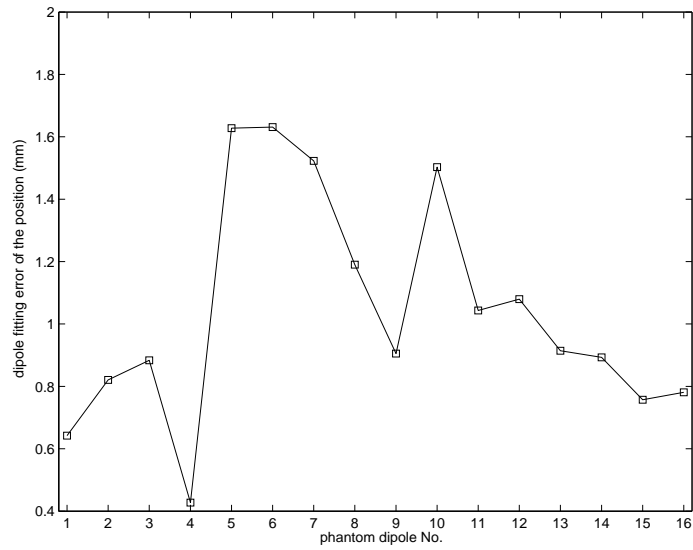
Figure 4.4: Dipole fitting error for checking the accuracy of Sarvas forward model by phantom experiment. Sixteen tangential phantom dipoles with different position are conducted and each is averaged by 50 trails. It uses the least square dipole fitting method involving the Sarvas forward model to localize the position of those dipoles. The average localization error is about $1mm$ which is no great difference with the prior studies [34, 37, 44].

and the standard deviation of the sensor noise is that of the empty room noise times 0.01. We estimate the source at the ground truth position by maximum contrast beamformer. It repeats the simulation 15 times for the pairs of the conditions that is with and without adding the regularization term. All of the 15 paired times are under the resistent that the condition number, with infinite norm, of the matrix $\mathbf{Q}'$ is greater than 10^{14} for preventing from ill-pose under that mantissa part is represented by 52 bits [6]. Here, the condition number is computed by

$$K = \|\mathbf{Q}'\|_\infty \|\mathbf{Q}'^{-1}\|_\infty, \tag{4.1}$$

where $\|\cdot\|_\infty$ denotes infinite norm. The β is set the trace of the matrix $\mathbf{Q}'$ times 10^{-10} which is far greater than the minimum value to prevent ill-condition that discussed in Chapter 2. The results are showed in Table 4.1 illustrating the difference estimated orientation between this two condition. We can find that the average influence of the regularization is about $0.00008°$ which just be about 1 percentage of the error between the estimated and true source orientations. By the discussion in 3.2.4 and the results here, we can say that a

proper β value is able to not only let $\mathbf{Q}$ (Υ) in Eq. 3.29 (Eq. 3.72) free from ill-condition but cause very less influence to the result under a sufficient accurate representation (double-precision) of the floating-point number.

4.1.3 Imaging of Source Power and Coherent Sources

Here, we use maximum contrast beamformer and maximum normalized correlation beamformer to respectively image the source power and time-frequency coherent sources in a putative source space by simulation. We put three targeted sources in the source space, their time course waveform, time-frequency map and the relative location are shown in Figure 4.5. The three sources are all locates at the scanning points of the beamformer. It notes that source1 and source2 are partial coherent in the time-frequency domain and spatially they differ from about 2.2 cm. Here the overlapping brain image is just for giving a roughly guide of the ratio of the distance between the sources and that of different brain areas. Three thousands noise sources are added and whose standard deviation is $10nAm$. Furthermore, the standard deviation of sensor noise is 0.1 times that of the empty room recordings. The regulator α is set be 0.0003, and the control, active states are $-1 \sim 0$ sec. and $0 \sim 1$ sec. respectively. Besides, the band pass filtering ($1 \sim 20$ Hz) is applied to the recordings for preprocessing; the ROI of the wavelet is $0 \sim 1$ and $1 \sim 20$Hz for imaging the time-frequency coherence and we let source1 be the reference signal. The processing flow to imaging the dynamic coherence is as the description in 3.3.4. except that here we just one trial because the putative source is deterministic. The results in Figure 4.6 and Figure 4.7) respectively shows that

**I.** The local maximum source significance are exactly at the ground truth positions of source1, 2 and 3.

II. The local maximum time-frequency coherence are exactly at the ground truth positions of source1, 2.

That is the proposed algorithm can be used to find out the sources (source1,2 and 3) with significant power (variance) and the coherent sources(source1 itself and source2) in Morlet wavelet domain.

Table 4.1: The table shows the effect of the regularization term β. Fifteen dipoles with randomly-assigned orientations are conducted. It uses maximum contrast beaformer to estimate the target source with the simulating recordings. "A" stands for the difference of the estimated orientation between the condition that the regularization term $\beta\mathbf{I}$ in Eq. 3.29 is added or not. "B" stands for the difference of the estimated orientation between the orientation of the ground truth and that of the estimated target source when no addition of β.

	A	B	A/B
orientation #01	0.000162	0.034032	0.476%
orientation #02	0.000081	0.021846	0.371%
orientation #03	0.000162	0.002132	7.600%
orientation #04	0.000081	0.010810	0.750%
orientation #05	0.000123	0.004290	2.861%
orientation #06	0.000000	0.016597	0.000%
orientation #07	0.000162	0.013815	1.173%
orientation #08	0.000081	0.009212	0.879%
orientation #09	0.000081	0.004871	1.663%
orientation #10	0.000125	0.010865	1.147%
orientation #11	0.000000	0.001658	0.000%
orientation #12	0.000000	0.004648	0.000%
orientation #13	0.000001	0.043497	0.003%
orientation #14	0.000056	0.029248	0.191%
orientation #15	0.000081	0.018119	0.447%
mean	0.000080	0.015043	1.171%
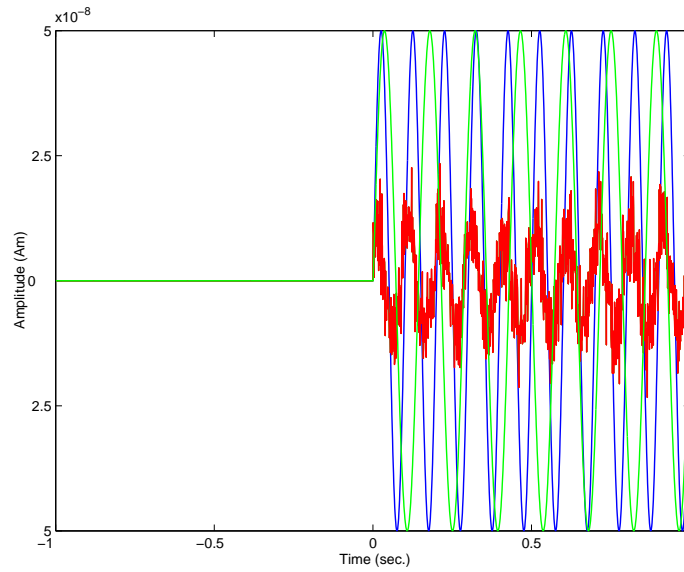
(a)
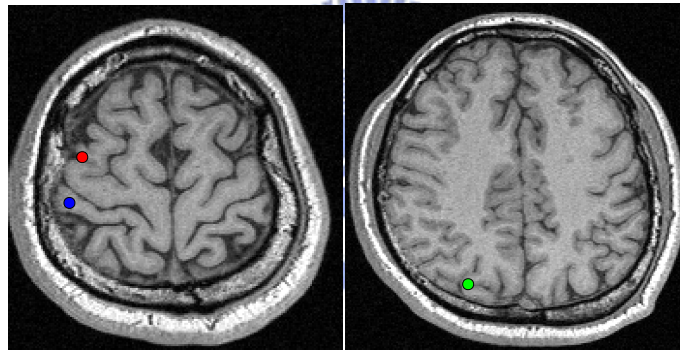
(b)

Figure 4.5: Computer generated sources for simulation.(a) The waveform of the three sources. All of they are zero from -1 sec. to 1 sec. Source1 (blue line) is a 10Hz sine wave in the period of $0 \sim 0.5$ sec. and is 15Hz in the period of $0.5 \sim 1$ sec.. Its amplitude is 50nAm. Source2 (red line) is similar with the source1 except that its amplitude is smaller (10nAm) and the phase is shifted $\pi/4$ from source1. Besides, source2 is also smeared by white noise (standard deviation: 5nAm). Source1 and source2 are partial coherent in the time-frequency domain. Source3 (green line) is a 16Hz sine wave in the period of $0 \sim 0.5$ sec. and is 7Hz in the period of $0.5 \sim 1.5$ sec. with the amplitude 50nAm.(b) The location of three sources. The locations of source1, 2 and 3 are represented by blue, red and green point respectively. The distance between source1 and source2 is about 2.2 cm and they are located on the same slice in the MR image of the putative head.
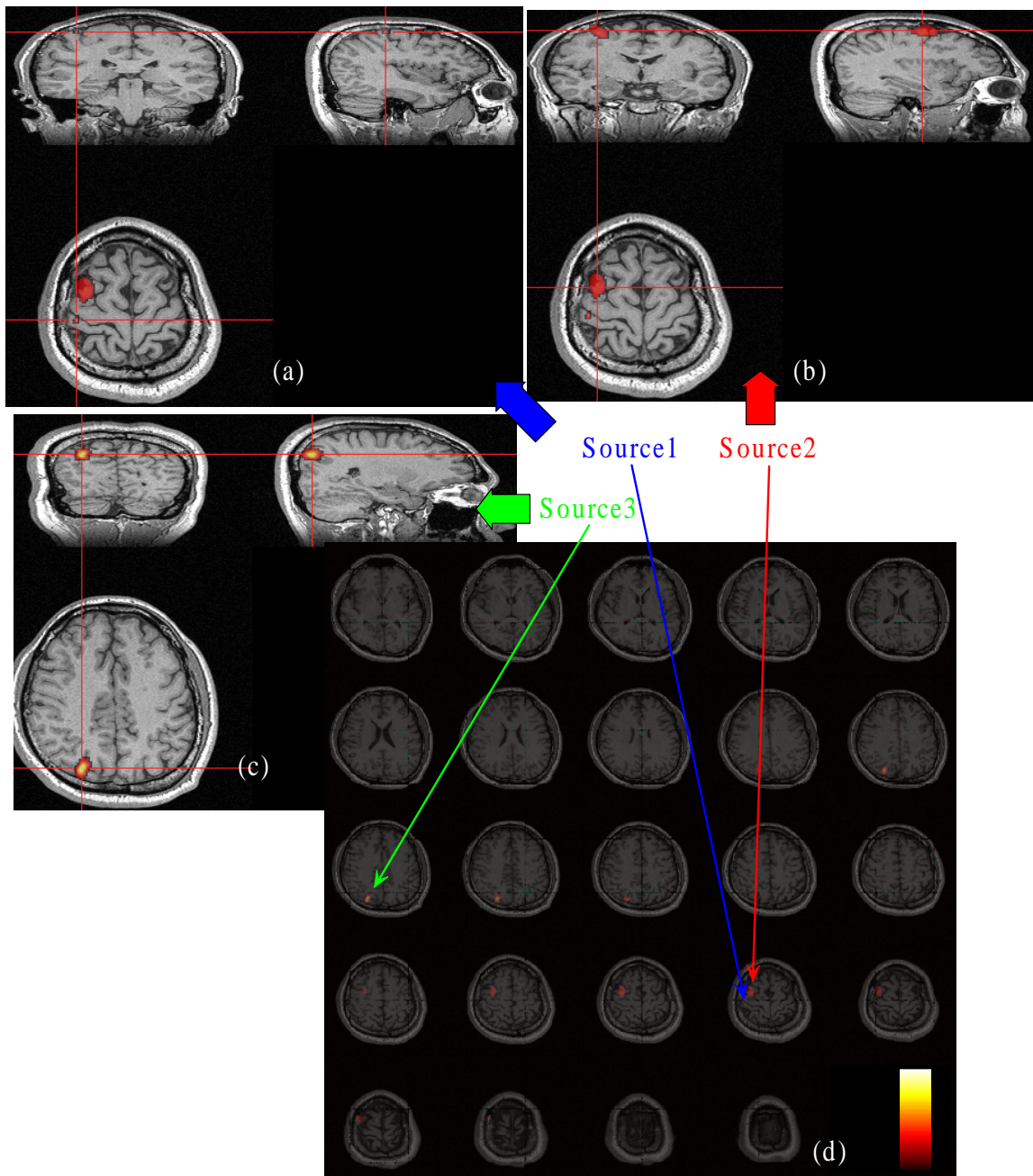
Figure 4.6: F-static map of the estimated source by maximum contrast beamformer with the simulated recordings. Three significant sources are simulated in the source space.(a)(b)(c) Estimated results are viewed form sagittal, coronal and transverse view aimed at the location of the putative source1, 2, 3.(d)Viewing the whole source space slice by slice. The map is normalized and truncated the part lower than 0.27 times the maximum value in the map.
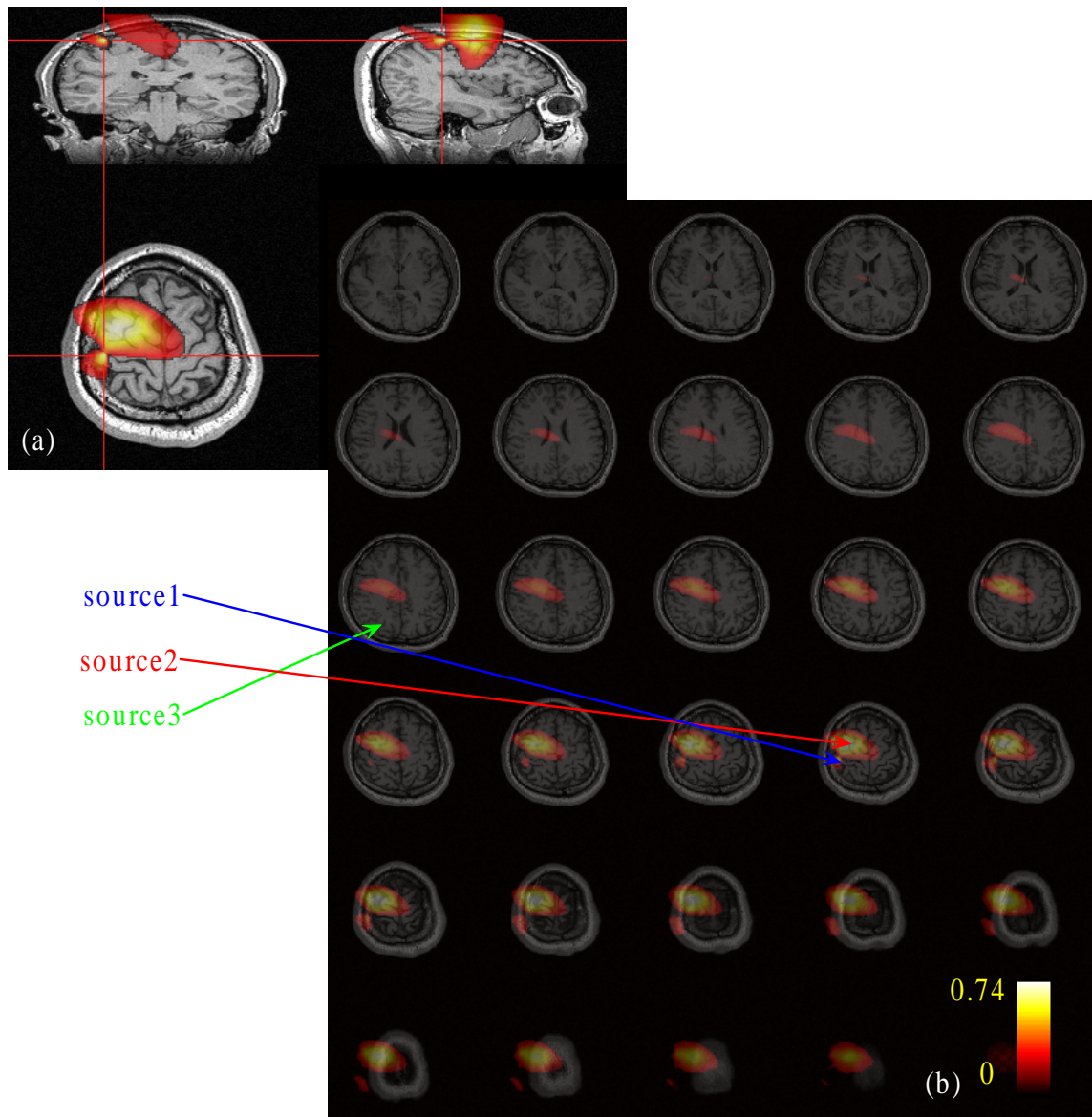
Figure 4.7: Time-frequency coherence map of the estimated sources by maximum normalized correlation beamformer with the simulated recordings. Three significant sources are simulated in the source space, where source1 is the reference signal and source2 are partially coherent with it in time-frequency domain. (a) Estimated results are viewed form sagittal, coronal and transverse view aimed at the location of the putative source1.(b)Viewing the whole source space slice by slice. The true location of the given source1, 2 and 3 are at the head of the blue, red and green arrow respectively. The map is truncated the part where the coherence is lower than 0.2.

4.1.4 Estimation of Source Orientation by Maximum Contrast Beam-fomer

We declared that our method has the ability to find an optimal solution of the source ordination. Here, we conduct the simulation and phantom experiment to show this ability. In the simulation, it sets a single source dipole, source1 described in the previous subsection. We separate the conditions that the orientation of targeted source is constrained on tangential plane or not. Parameters of the target source are the same as the last experiment. We add zero-mean 3000 noise sources with the standard deviation $1/5$ times the amplitude of the target source. The sensor noise is added with the standard deviation varying from 0.01 ,0.1 to 1 times that of the empty room data. Because the regularization term $alpha$ is relative to the SNR, we vary it in all conditions from the value of 0.00003, 0.0003 to 0.003 times the maximum eigenvalue of the covariance matrix of active state. Band pass filter ($1 \sim 20$Hz) and baseline correction are adapt in preprocessing. It demonstrates the resultant mean error and standard deviation under 15 generated dipoles for each condition in Figure 4.8 and Figure 4.9 respecting the randomly given orientation are with one degree of freedom on the tangential plane and are with two in the three dimensional space. It should note that we estimate the orientation of the source with two degree of freedom in three dimensional spaces in both cases. In the phantom experiment, the phantom source dipole is set to be a 16.67 Hz sine wave with the amplitude of 50nAm. We use band pass filter to filter out the recording signals other than $1 \sim 20$ Hz and than average 50 trials. Sixteen dipoles are conducted and then we compute the average error of the estimated dipole orientations at the position where the estimated F-statistic is maximum (the average difference between the position with maximum F-statistic and the ground truth of phantom dipole position is 1.6381 ± 0.4971 mm). Here, α is 0.0003. The result shows in Figure 4.10.

When we constrain the given source on the tangential plane, the simulation shows that the estimated orientation error is under $2°$ when the regulator α are set properly. Similar results are also showed in the phantom experiment that the average error cross each dipole is also about $2°$. The average difference between the true dipole orientation and the closer targeted direction in the LCMV-based method is $45/2 = 22.5$ degree when the dipole is constrained in the tangential plane. In short, The two results from simulation and

phantom experiments show that our method indeed can find accurate source orientation for beamformer.

As the source is not constrained on the tangential plane, error not only increases significantly but is more unstable. This can be explained by the effect that MEG is more sensitive to the tangential source than the radial one. That is, the radial component of a source cause small contribution to the recordings so that the SNR of the radial part is small. Therefore, the radial part of the estimated source orientation will be more unstable and that cause the larger estimation error. For verifying this explanation, we conducted an other simulation varying the angle $(0°, 15°, 30°, 45°, 60°, 75°, 90°)$ between the dipole orientation and the tangential plane. Here, sensor noise is 0.1 time and α is 0.0003. The result (Figure 4.11) shows the error is approximately caused by the angle aberrant from tangential plane. Hence, we can say that the error in the case is greatly caused by the intrinsic property of the MEG modality rather than the inverse algorithm.

4.1.5 Estimation of Source Orientation by Maximum Normalized Correlation Beamformer

Very similar to the verification of the estimated source orientation of maximum contrast beamformer, here we verify another proposed algorithm, maximum normalized correlation beamformer, by simulation in the Morlet wavelet domain. The source, noise and preprocessing configuration of the simulation is the same as that for maximum contrast beformer. We use the true target source as the reference source and hence it purposely has the maximum coherent with itself. The processing follows the description in 3.3.4. except that here we just one trial because the putative source is deterministic. We probe the source at the exact position of the target source and compute the average estimated source orientation error, which illustrates in Figure 4.12.

The result shows that the average error is about $2 \sim 3$ degree dependent on different noise level when the regularization term α is set properly. Thus, we can say that the algorithm can find a proper source direction by the maximum normalized correlation criteria. Besides, either in the this case or the case of the maximum contrast beamformer, we can find that setting a proper regularization term α is important. However, unfortunately,
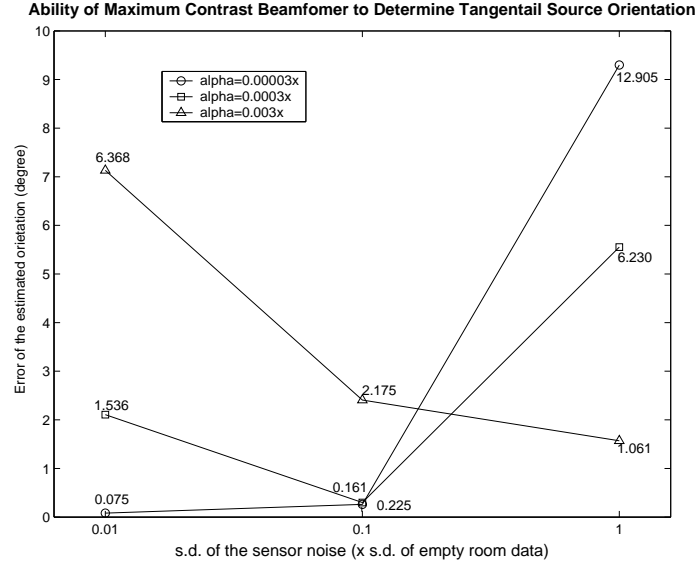
Figure 4.8: The mean error and the standard deviation of the estimated orientation of 15 simulated target sources by maximum contrast beamformer under different sensor noise level with varying the regularization term α. The target source orientation is resisted in the tangential plane i.e. with one degree of freedom. Each line shows the results with one alpha value cross the standard deviation of sensor noise from 0.01, 0.1 to 1 times that of the the empty room data. The alpha value are vary from 0.00003, 0.0003 to 0.003 times the maximum eigenvalue of the data covariance matrix. Y-axis represents the mean error and the numbers neighboring each mark does the standard deviation under that condition.

there is still difficult to determine this value both properly and full-automatically because it depends on the source configuration as we mentioned before.

4.1.6 Computational Cost of the Proposed Algorithms

Theoretically, SAM can find the same source orientation as the proposed maximum contrast beamformer, when SAM is extended to 3D and infinitely sample and exhaustively search the orientation solution space. Even, by similar way, it also can find a source orientation with maximum normalized correlation like proposed maximum normalized correlation beamformer. The advantage of our method over SAM is that ours has lower computational cost. In the following, we compare the computational time between the parts that is different in ours algorithm and SAM. To avoid trapping into local minimums, here, we assume
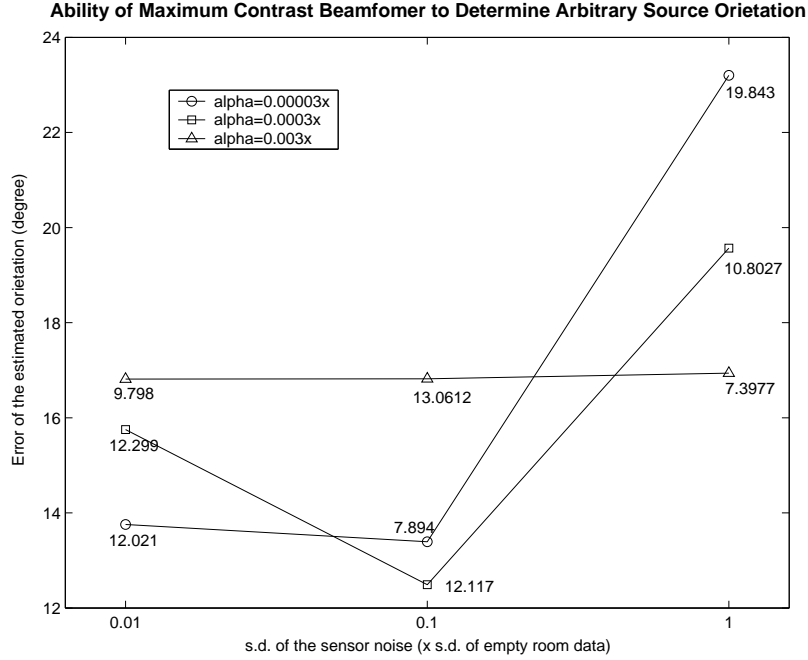
Figure 4.9: The mean error and the standard deviation of the estimated orientation of 15 simulated target sources by maximum contrast beamformer under different sensor noise level with varying the regularization term α. The target source orientation is arbitrary in the 3D space i.e. with two degree of freedom. Each line shows the results with one alpha value cross the standard deviation of sensor noise from 0.01, 0.1 to 1 times that of the the empty room data. The alpha value are vary from 0.00003, 0.0003 to 0.003 times the maximum eigenvalue of the data covariance matrix. Y-axis represents the mean error and the numbers neighboring each mark does the standard deviation under that condition.

the SAM exhaustively search the optimal solution.

The different part of the proposed algorithms from SAM is at Eq. 3.29 where we derive the estimated source orientation $\mathbf{j}$ by solving an eigen problem while SAM exhaustively substitute different testing $\mathbf{j}$s into the objective function for finding a $\mathbf{j}$ such that the the objective value is maximum. We compare the computational time of this part in these two approaches. The assumption that the testing $\mathbf{j}$s in SAM are predefined is adapted, that is, it assumes SAM spending no time to compute the $\mathbf{j}$s. We repeat the procedure 100000 times, for the simulation of the condition that probing 100000 positions in the source space. It dose on a computer equipping the CPU of AMD Athlon(TM) XP 3000+ (clock rate: 2.17GHz) and 512 MB RAM. Besides, the program is optimized to maximum speed by
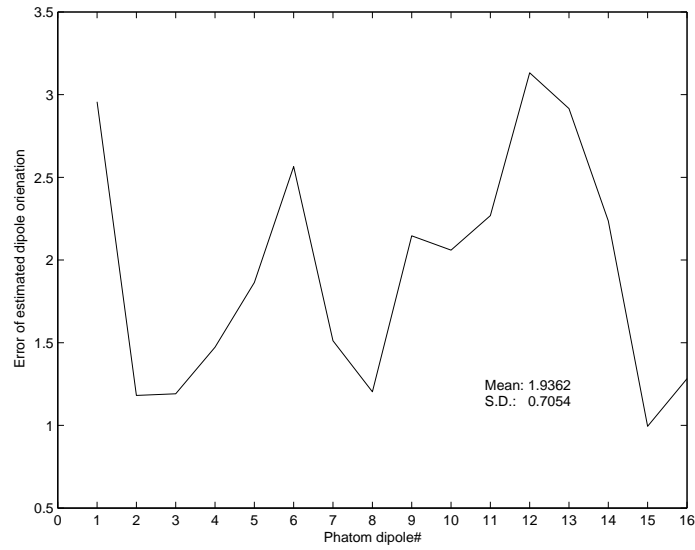
Figure 4.10: The error (y-axis) of the estimated orientation of 16 phantom dipoles (x-axis) with varying the regularization term α (black line) by maximum contrast beamformer. The phantom source dipole is set to be a 16.67 Hz sine wave with the amplitude of 50nAm. We use band pass filter to filter out the recording signals other than $1 \sim 20$ Hz and than average 50 trials. The average error of the estimated dipole orientations is computed at exactly the position where the true dipoles locate. We also compute average error and standard deviation the in the best condition of each dipole (blue line).

compiler and all floating point numbers are represented by complex number for generality The pseudo-code of the parts of our algorithm and SAM for this comparison are listed in the following respectively.

Comput_Time_Compar_ProposedMethod($\mathbf{P}$, $\mathbf{Q}'$)

1   **begin**

2         $startTime := getTime()$

3   **for** $i := 1$ **to** 100000 **do**

4   **begin**

5                 $\beta := trace(Q') \times 10^{-10}$

6                 $\mathbf{Q^{-1}} := inverse(\mathbf{Q} + \beta\mathbf{I})$

7                 $\lambda_{max} := maxEigVal(\mathbf{Q^{-1}P})$

8                 $\tilde{\mathbf{j}} := eigVec(\lambda_{max}, \mathbf{Q_{-1}P})$
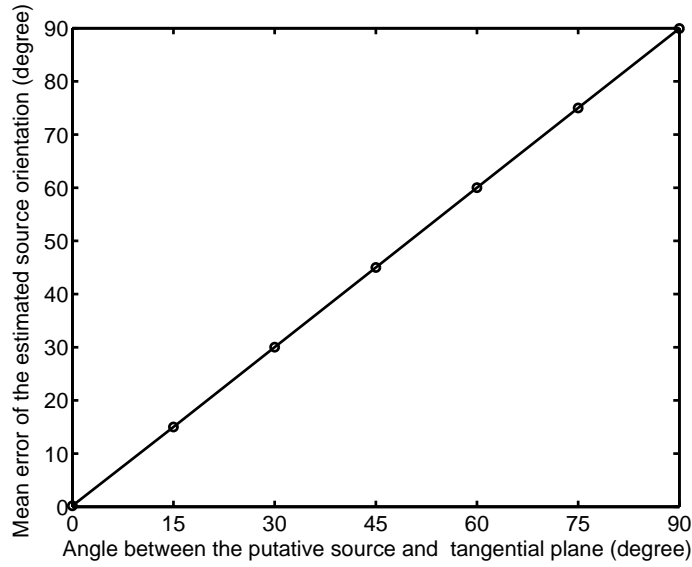
Figure 4.11: The effect of the radial component of dipole source upon estimated dipole orientation. Y-axis represents the mean error of the estimated orientation of 15 simulated target sources by maximum contrast beamformer. The angle between the target source orientation and the tangential plane is vary from $0°$ to $90°$ with the interval $15°$ (x-axis).

9   **end**

10       $endTime := getTime()$

11   **return** $endTime - startTime$

12   **end**

$Comput\_Time\_Compar\_SAM(\mathbf{P}, \mathbf{Q}')$

13   **begin**

14       $startTime := getTime()$

15   **for** $i := 1$ **to** 100000 **do**

16   **begin**

17         $maxVal := 0$

18         $maxIndex := 1$

19   **for** $k := 1$ **to** K **do**

20   **begin**

21            $tmpVal = \frac{\mathbf{j}_k{}^T \mathbf{P} \mathbf{j}_k}{\mathbf{j}_k{}^T \mathbf{Q}' \mathbf{j}_k}$
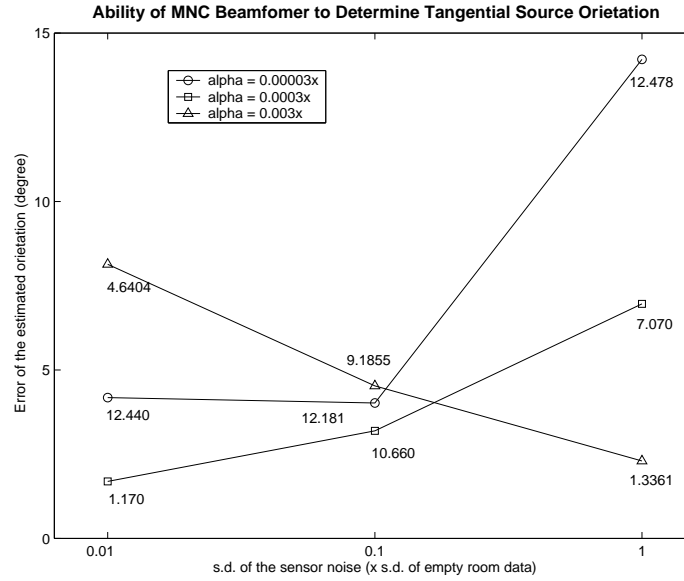
Figure 4.12: The mean error and the standard deviation of the estimated orientation of 15 simulative target sources differing orientation by maximum normalized correlation beamformer under different sensor noise level with varying the regularization term α. The target source orientation is resisted in the tangential plane i.e. with one degree of freedom. Each line shows the results with one alpha value cross the standard deviation of sensor noise from 0.01, 0.1 to 1 times that of the the empty room data. The alpha value are vary from 0.00003, 0.0003 to 0.003 times the maximum eigenvalue of the data covariance matrix. Y-axis represents the mean error and the numbers neighboring each mark does the standard deviation under that condition.

22	**if** $maxVal < tmpVal$ **do**
23	**begin**
24	$maxVal := tmpVal$
25	$maxIndex := k$
26	**end**
27	**end**
28	$\tilde{\mathbf{j}} = \mathbf{j}_{maxIndex}$
29	**end**
30	$endTime := getTime()$
31	**return** $endTime - startTime$

32   **end**

The procedure $inverse(), maxEigVal()$ and $eigVec()$ at line 6, 7 ,and 8 compute the inverse matrix, maximum eigenvalue of a matrix ,and the eigenvector of a given matrix and a given eigenvalue respectively by the methods introduced in 3.2.4. The utilization of the code at line $23 \sim 26$ is to record the index of the estimated source orientation associating the maximum contrast. The K at line 19 is the total probing orientation number of SAM for one position. Here, we set $K = 180/5 = 36$ as SAM probing the direction (axis) constraint in a 2D plane and set $K = (180/5) \times (360/5) = 2592$ for whole 3D space. That is, we set $5°$ as the directional probing resolution of SAM. The results are showed in Table 5.1. It notes that the LCMV spends no time in this part.

From the results, we can find that the computational time of our method is about $1/3$ times that of SAM as it probes each 5 degree in a 2D plane and does the exhaustive search. If we extend SAM to probe in 3D space that match the ability of our method, the ratio is $1 : 218$. Even the resolution of our method as showed in previous simulation and phantom experiment is smaller than this setting of SAM. The cost of SAM will be proportional to the directional probing resolution when probing in 2D plane (with one degree of freedom) or to the square of the probing resolution when probing in 3D space (with two degrees of freedom). In short, our method overcomes the drawback, high computational cost, of SAM, especially when the directional probe is performed in the whole 3D space.

4.2   Experiment of Self-paced Finger Movement

Human experiment is the most real case to check the algorithms for true applications. However, it needs to notes that we just can find reasonable explanations to the results by the already-known knowledge in neuropathology. it is due to that we never have the ground truth of the neuron activities in a human brain. That is, the problem always have no exact answers. If we have the ground truth, we have no need to pay a lot of efforts to solve the inverse problem for imaging the brain activation.

Here, we apply proposed methods to human experiments of self-paced finger move-

Table 4.2: Comparison of SAM and proposed approach in computing time. We compare the computational time between the parts that is different in our algorithm and SAM. We repeatedly execute the procedure of this part 100000 times, for the simulation of the condition that probing 100000 positions in the source space. The program optimized by compiler runs on the CPU of AMD Athlon(TM) XP 3000+ (clock rate: 2.17GHz). The pseudo-code for the comparison can be found in *Comput_Time_Compar_ProposedMethod()* and *Comput_Time_Compar_SAM()*. Here, we set $5°$ as the directional probing resolution of SAM and respectively list its results in $2nd$ and $3rd$ rows for the original SAM and the extension to probe direction in whole 3D space. The last row lists the result derive by our method. We use ' and " to denote minute and second respectively. Beside, it notes that the LCMV-based algorithm spends no time in this part, which is list in the first row.

	Time
LCMV (3D)	0' 0"
SAM (2D, $5°$)	0' 3.953"
SAM (3D, $5°$)	4' 42.269"
Our (3D)	0' 1.296"

ment. A subject spontaneously lift her left/right index finger and the task is repeated 100 times (100 trials) for derive sufficient statistic. The data is recorded by the MEG sensors with the sampling rate of 250 Hz and preprocessed through the steps of EOG rejection, SSP, band pass filtering ($3 \sim 35$Hz), and baseline correction.

We apply the maximum contrast beamformer to estimate the brain activities and maximum normalized correlation beamformer to estimate the coherent areas in the brain. In the first case, the average data cross 100 trials is adapted. Then, we set the active state as the period of $-0.12 \sim 0.36$ sec., where 0 is the exact time that finger lifts and the control state covariance matrix are estimate by the empty room recordings with the assumption that the noise on each sensor are independent. The Results are illustrates in Figure 4.13 and Figure 4.14 for left and right finger lifting respectively. In second case, we use the estimation at the location with the maximum F-statistic value as reference signal and then exploits the procedure introduced in 3.3.4 to imaging the time-frequency coherent sources. The ROI of the wavelet coefficients is chosen from $-1 \sim 1$ sec. in time domain and $8 \sim 25$ Hz in frequency domain. Figure 4.15(a) and Figure 4.16(a) are the selected time-frequency

power spectrum maps of the reference point for left and right index finger lifting experiments respectively. The Results of the coherence level in whole source space are illustrates in Figure 4.15(b) and Figure 4.16(b) respectively.

From the first result, we can find that the location of the maximum value locates at the place is near the hand sensorimotor cortex area, which fits the neuropathological knowledge. Another, form Figure 4.15 and Figure 4.16, we can find that the coherence map shows that the estimated signals at the areas near sensorimotor cortex, secondary motor and dorsolateral areas are coherent with the reference signal. These areas are correlated with motor task.
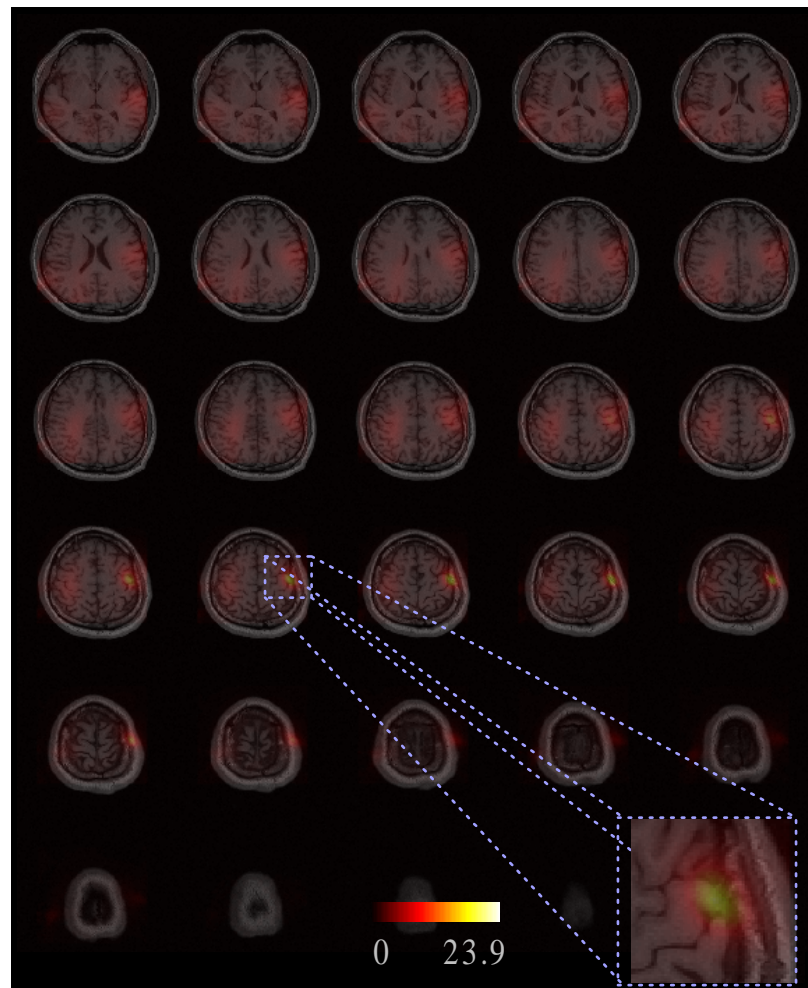
Figure 4.13: F-statistic map of the estimated sources by maximum contrast beamformer with the recordings from left index finger movements experiment.
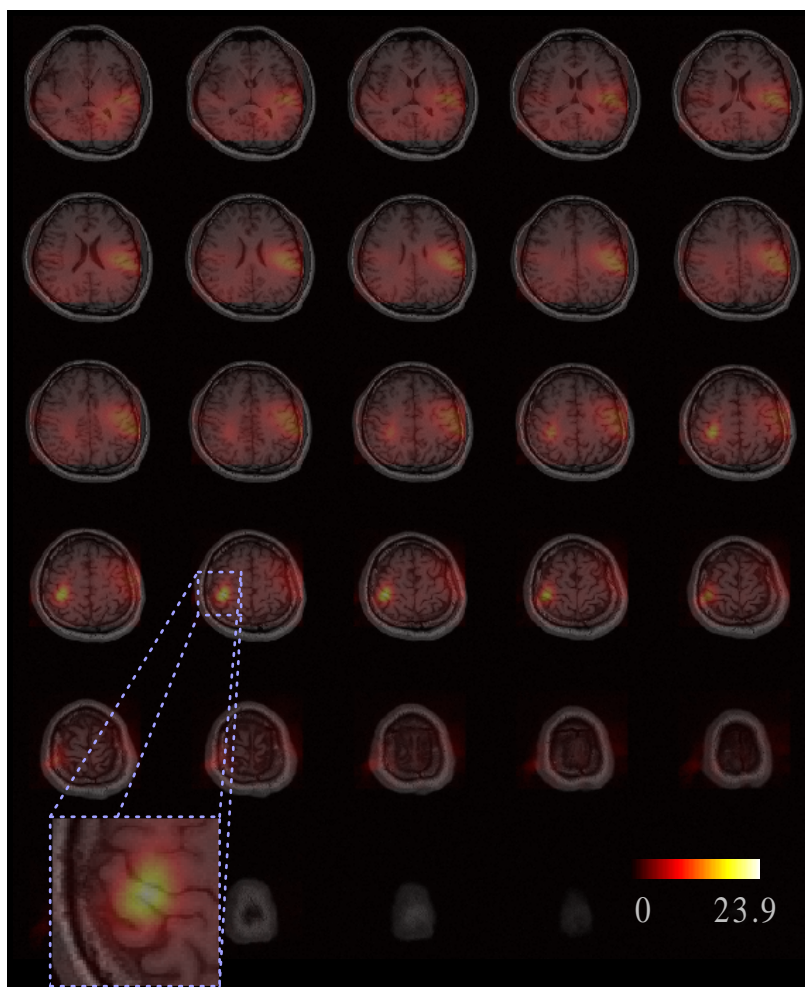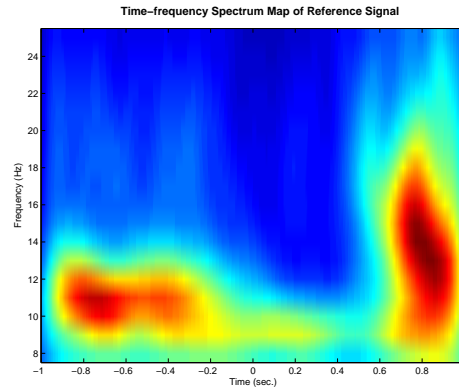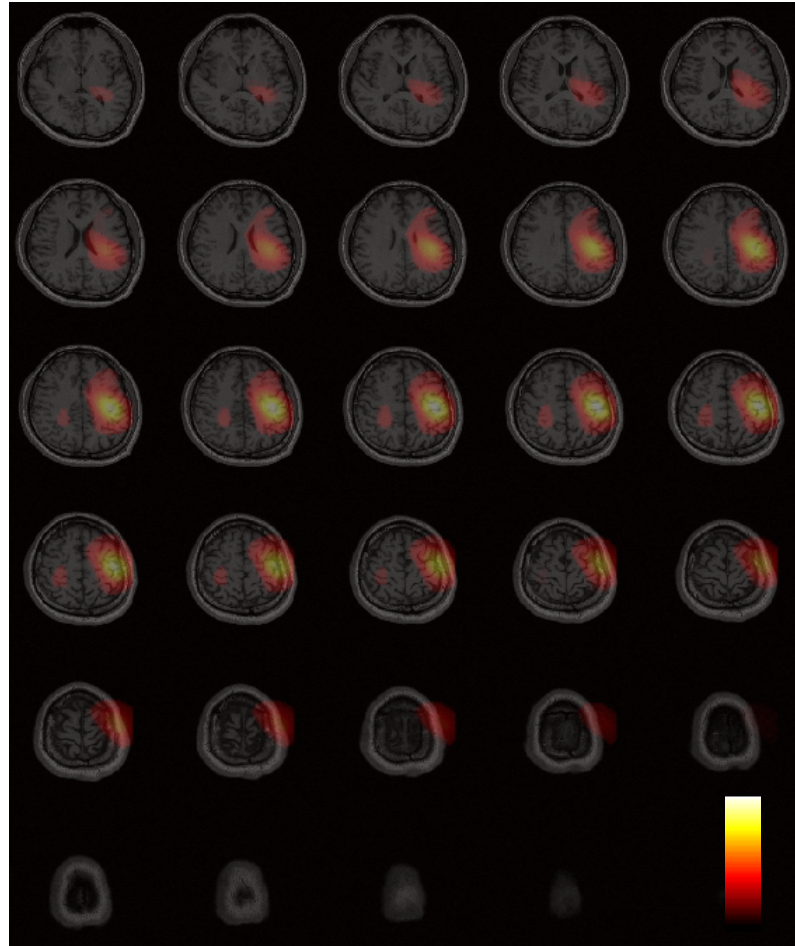
Figure 4.14: F-statistic map of the estimated sources by maximum contrast beamformer with the recordings from right index finger movements experiment.

(a)

(b)

Figure 4.15: Time-frequency Coherence map of the estimated sources by maximum normalized correlation beamformer with the recordings from left index finger finger movements experiment. The map is normalized and truncated the parts that their coherence is lower than 0.2. We use the estimation at the location with the maximum F-statistic value as reference signal and then exploits the procedure introduced in 3.3.4 to imaging the time-frequency coherent sources. (a)Power spectrum of Morlet wavelet representation of reference signal (ROI of the wavelet coefficients) (b)Viewing coherent level in whole source space slice by slice.
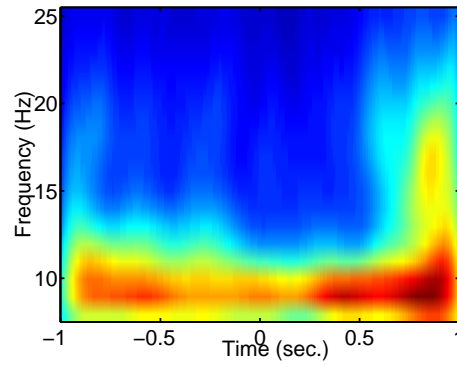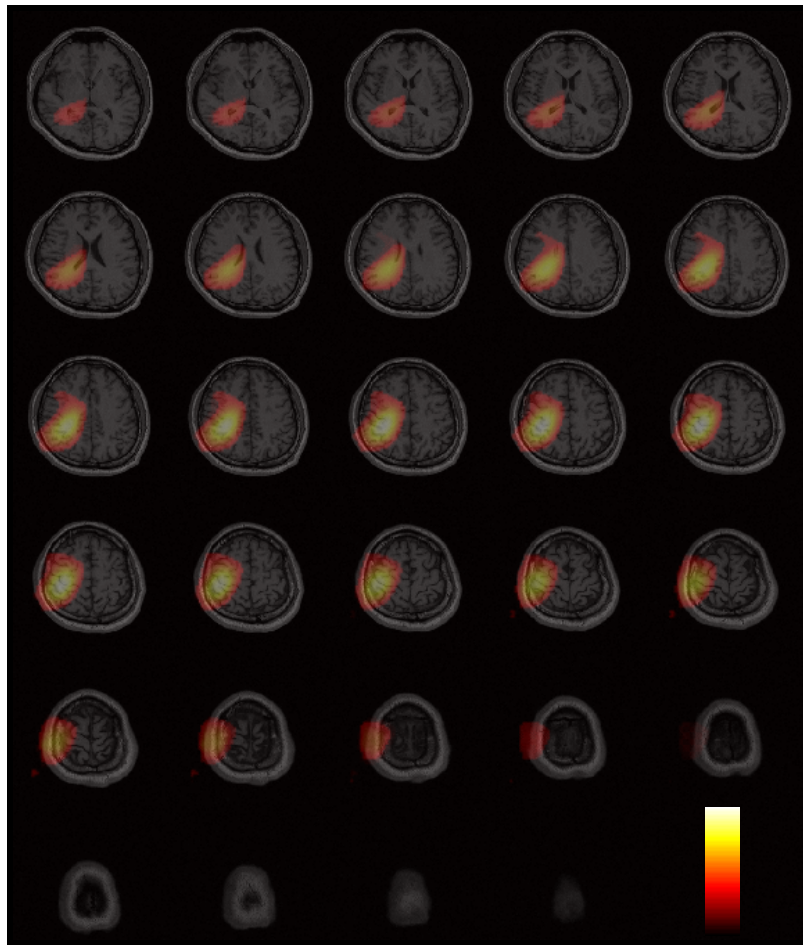
(a)

(b)

Figure 4.16: Time-frequency Coherence map of the estimated sources by maximum normalized correlation beamformer with the recordings from right index finger finger movements experiment. The map is normalized and truncated the parts that their coherence is lower than 0.2. We use the estimation at the location with the maximum F-statistic value as reference signal and then exploits the procedure introduced in 3.3.4 to imaging the time-frequency coherent sources. (a)Power spectrum of Morlet wavelet representation of reference signal (ROI of the wavelet coefficients) (b)Viewing coherent level in whole source space slice by slice.

Chapter 5

Conclusions

In 3.2.4, we proposed maximum contrast beamformer which determines a meaningful source orientation that maximizes the F-statistic value. The criteria is similar with SAM such that it has no probability of miss-detection that LCMV-based approaches may encounter. Rather than (exhaustively) searching, our method determines the source orientation via solving an eigen problem of a 3×3 matrix. The problem can be solved by deterministic steps including just primary arithmetic and matrix computational operations, that is, the computational complexity is merely $O(1)$.

In 3.3.3, we proposed another algorithm, maximum normalized correlation beamformer, to image the coherent sources. The algorithm is like DICS but, first, we use the technique that is similar to maximum contrast beamformer to analytically determine a proper direction (maximum normalized correlation) for probing and, second, it, theoretically, can image the sources which correlate in the domain where the auto- and cross- correlation are defined.

In 3.3.4, we utilized maximum normalized correlation beamformer and provide a procedure to image the time-frequency coherent sources that may be coherent cross multiple band by computing the auto- and cross- correlation on the selected Morlet wavelet domain. First we transform the reference signal from time course representation to the time-frequency representation by Morlet wavelet coefficients among which we select the interesting coefficients. After the same step is applied to the recordings, we estimate the auto- and cross- correlation matrix by average that of very trials. Finally, feed auto- and cross- correlation matrix into the maximum normalized correlation beamformer to estimate the coherence between the target position and the reference signal.

In Chapter 4, the simulation, phantom experiments were conducted to generate recordings with the ground truth for verification and demonstration of the proposed methods. According to the results, we can find that, indeed, they can accurately find the orientation of the targeted source with low computational cost. Table 5.1 gives a summarized comparison between our, LCMV-based, SAM methods in the issues of accuracy and efficiency. Also, proposed methods respectively image reasonable maps of the significance of the source power and coherent sources in the head by feeding the simulated recordings. Besides, we apply our method to the recordings measured from real finger movement experiment and the results approximates fit the already-known neuropathological knowledge.

Table 5.1: Comparison of SAM, LCMV and our methods in both computational cost and robustness. "Our" stands for our methods including maximum contrast and maximum normalized correlation beamformers. "SAM_3D" stands for the extension of the SAM that probing the direction in 3D space, that is, with two degree of freedom like the ability of "Our" and "LCMV".

	Comparison of different methods
Accuracy	Our $\geq$ SAM_3D $>$ LCMV
Efficiency	LCMV $>$ Our $>$ SAM $>>$ SAM_3D

Bibliography

[1] C. Andrew and G. Pfurtsheller. Ecent-related coherence as a tool for studying dynamic interaction of brain regions. *Electroencephalogr. Clin. Neurophysiol.*, 98:144–148, 1996.

[2] S. Baillet, J. C. Mosher, and R. M .Leahy. Electromagnetic brain mapping. *IEEE Signal Proc. Mag.*, pages 14–30, Noveber 2001.

[3] E. Basar, C. Basar-Eroglu, S. Karakas, and M. Schurmann. Oscillatory brain theory: a new trend in neuroscience. *IEEE Eng. Med. Biol. Mag.*, 18(3):56–66, May-June 1999.

[4] S. L. Bressler, R. Coppola, and R. Nakamura. Episodic multiregional cortical coherence at multiple frequencies during visual task performance. *Nature*, 366:153–156, November 1993.

[5] E. N. Bruce. *Biomedical Signal Processing*. Wiley, 2001.

[6] R. L. Burden and J. D. Faires. *Numerical Analysis*. Brooks Cole, 7th edition, 2000.

[7] D. Cheyne, G. R. Barnes, I. E. Holliday, and P. L. Furlong. Localization of brain activity associated with non-time-locked tactile stimulation using synthetic aperture magnetometry (SAM). In *12th International Conference on Biomagnetism*, Espoo, Finland, Augist 2000.

[8] E. K. P. Chong and S. H. Zak. *An Introduction to Optimization*. Wiley, 2nd edition, 2001.

[9] A. Cohen and J. Kovacevic. Wavelets: The mathematical background. *Proceedings of the IEEE*, 84(4):514–522, April 1996.

[10] L. Cohen. *Time-Frequency Analysis*. Pentice Hall, 1995.

[11] T. H. Corman, C. E. Leiserson, R. L. Rivest, and C. Stein. *Introduction to Algorithms*. MIT Press, 2nd edition, 2001.

[12] H. Cox, R. M. Zeskind, and M. M. Owen. Robust adaptive beamforming. *IEEE Trans. Acoust., Speech, Signal Processing*, ASSP-35(10):1365–1376, October 1987.

[13] O. David, L. Garnero, D. Cosmelli, and F. J. Varela. Estimation of neural dynamics from MEG/EEG cortical current density maps: Application to the reconstruction of large-scale cortical synchrony. *IEEE Trans. Biomed. Eng.*, 49(9):975–987, September 2002.

[14] A. Delorme and S. Makeig. EEGLAB: an open source toolbox for analysis of single-trial EEG dynamics including independent component analysis. *J. Neurosci. Methods.*, 134:9–21, 2004.

[15] J. J. Ermer, J. C. Mosher, S. Baillet, and R. M. Leahy. Rapidly re-computable EEG forward models for realistic head shapes. *Phys. Med. Biol.*, 46(4):1265–1281, April 2001.

[16] W. C. Gaetz and D. O. Cheyne. Localization of human somatosensory cortex using spatially filtered magnetoencephalography. *Neurosci. Lett.*, 340:161–164, 2003.

[17] S. Ghahramani. *Fundamentals of Probability*. Prentice Hall, 3rd edition, 2000.

[18] R. Goldenberg, R. Kimmel, E. Rivlin, and M. Rudzsky. Cortex segmentation: A fast variational geometric approach. *IEEE Trans. Med. Imaging*, 21(12):1544 – 1551, DECEMBER 2002.

[19] R. C. Gonzalez and R. E. Woods. *Digital Image Prcessing*. Prentice Hall, 2nd edition, 2001.

[20] R. P. P. P. Grasman, H. M. Huizenga, L. J. Waldorp, K. B. E. Bocker, and P. C. M. Molenaar. Frequency domain simultaneous source and source coherence estimation with an application to MEG. *IEEE Trans. Biomed. Eng.*, 51(1):45–54, JANUARY 2004.

[21] J. Gross and A. A. Ioannides. Linear transformations of data space in MEG. *Phys. Med. Biol.*, 44:2081–2097, 1999.

[22] J. Gross, J. Kujala, M. Hamalainen, L. Timmermann, A. Schnitzler, and R. Salmelin. Dynamic imaging of coherent sources: studying neural interactions in the human brain. *Proc. Natl. Acad. Sci. U.S.A.*, 98(2):694–699, January 2001.

[23] J. Gross, F. Schmitz, I. Schnitzler, K. Kessler, K. Shapiro, B. Hommel, and A. Schnitzler. Modulation of long-rang neural synchrony reflects temporal limmitations of visual attention in humans. *Proc. Natl. Acad. Sci. U.S.A.*, 101(35):13050–13055, 2004.

[24] J. Gross, L. Timmermann, J. Kujala, M. Dirks, F. Schmitz, R. Salmelin, and A. Schnitzler. The neural basis of intermittent motor control in humans. *Proc. Natl. Acad. Sci. U.S.A.*, 99(4):2299–2302, February 2002.

[25] J. Gross, L. Timmermann, J. Kujala, R. Salmelin, and A. Schnitzlera. Properties of MEG tomographic maps obtained with spatial filtering. *NeuroImage*, 19:1329–1336, 2003.

[26] M. Hamalainen and R. Ilmoniemi. Interpreting magnetic fields of the brain: minimum norm estimates. *Med. Biol. Eng. Comput.*, 32(1):35–42, 1994.

[27] M. S. Hamalainen, R. Hari, R. J. Ilmoniemi, J. Kuuutila, and O. V. Lounasmaa. Magnetoencephalography - theory, instrumentation, and applications to noninvasive studies of the working human brain. *Rev. Mod. Phys.*, 65(2):413–497, 1993.

[28] N. Hess-Nielsen and M. V. Wickerhauser. Wavelet and time-frequency analysis. *Proceedings of the IEEE*, 84(4):523–540, April 1996.

[29] A. Hillebrand and G. R. Barnes. The use of anatomical constraints with MEG beamformers. *NeuroImage*, 20:2302–2313, 2003.

[30] M. Huang, C. J. Aine, S. Supek, E. Best, D. Ranken, and E. R. Flynn. Multi-start downhill simplex method for spatio-temporal source localization in magnetoen-cephalography. *Electroencephalogr. Clin. Neurophysiol.*, 108:32–44, 1998.

[31] O. Jensen and S. Vanni. A new method to identify multiple sources of oscillatory activity form magnetoencephalographic data. *NeuroImage*, 15:568–574, 2002.

[32] M. Kaminski, K. Blinowska, and W. Szelenberger. Topographic analysis of coherence and propagation of EEG activity during sleep and wakefulness. *Electroencephalogr. Clin. Neurophysiol.*, 102:216–227, 1997.

[33] H. Krim and M. Viberg. Two decades of array signal processing research. *IEEE Signal Proc. Mag.*, pages 67–94, July 1996.

[34] H. Kwon, Y. H. Lee, J. M. Kim, Y. K. Park, and S. Kuriki. Localization accuracy of single current dipoles from tangential components of auditory evoked fields. *Phys. Med. Biol.*, 47:4145V4154, 2002.

[35] J. P. Lachaux, A. Lutz, D. Rudrauf, D. Cosmelli, M. L. V. Quyen, J. Martinerie, and F. Varela. Estimating the time-course of coherence between single-trial brain signals: an introduction to wavelet coherence. *Neurophysiol Clin.*, 32:175–174, 2002.

[36] D. C. Lay. *Linear Algebra and its applications*. Addison Wesley, 2nd edition, 1998.

[37] R. M. Leahy, J. C. Mosher, M. E. Spencer, M. X. Huang, and J. D. Lewine. A study of dipole localization accuracy for MEG and EEG using a human skull phantom. *Electroencephalogr. Clin. Neurophysiol.*, 107(2):159–173, August 1998.

[38] L. Leocani, C. Toro, P.Manganotti, P. Zuang, and M. Hallett. Event-related coherence and event-related desynchronization/synchronization in the 10 hz and 20 hz eeg dur-ing self-paced movements. *Electroencephalogr. Clin. Neurophysiol.*, 104:199–206, 1997.

[39] T. H. Li and W. R. Klemm. Detection of cognitive binding during ambiguous fig-ure tasks by wavelet coherence analysis of EEG signals. In *Proceedings of the 15th International Conference on Pattern Recognition*, Barcelona, Spain, September 2000.

[40] F. H. Lin, T. Witzel, M. S. Hamalainen, A. M. Dale, J. W. Belliveau, and S. M. Stufflebeam. Spectral spatiotemporal imaging of cortical oscillations and interactions in the human brain. *NeuroImage*, 23:582–595, 2004.

[41] H. Y. Liu, T. C. Lee, J. L. Hwang, C. Y. Cheng, Y. S. Chen, L. F. Chen, and J. C. Hsieh. Anatomy-constrained MEG beamformer for spatiotemporal imaging of brain activity. In *Biomedical Engineering Society of the ROC 2004*, Taiwan, 2004.

[42] V. K. Madisetti and D. B. Williams, editors. *The digital signal processing handbook.* CRC Press, 1997.

[43] K. Matsuura and Y. Okabe. Selective mimimum-norm solution of the biomagnetic inverse problem. *IEEE Trans. Biomed. Eng.*, 42(6):608–615, June 1995.

[44] E. Menninghaus, B. Lutkenhoner, and S. Gonzalez. Localization of a dipolar source in a skull phantom: Realistic versus spherical model. *IEEE Trans. Biomed. Eng.*, 41(10):986–989, October 1994.

[45] Microsoft Corp. *MSDN Library,* Visual Studio 6.0 edition.

[46] J. C. Mosher and R. M. Leahy. Source localization using recursively applied and projected (RAP) MUSIC. *IEEE Trans. Biomed. Eng.*, 47(2):332–340, February 1999.

[47] J. C. Mosher, R. M. Leahy, and P. S. Lewis. EEG and MEG: forward solutions for inverse methods. *IEEE Trans. Biomed. Eng.*, 46(3):245–259, March 1999.

[48] J. C. Mosher, P. S. Lewis, and R. M. Leahy. Multiple dipole modeling and localization from spatio-temporal MEG data. *IEEE Trans. Biomed. Eng.*, 39:541–557, June 1992.

[49] Neuromag Inc. *Source Modelling Software User's Guide*, May 2000.

[50] A. V. Oppenheim, R. W. Schafer, and J. R. Buck. *Discrete-Time Signal Processing*. Prentice Hall, 2nd edition, 1999.

[51] G. Pfurtscheller and F. H. L. D. Silva. Event related EEG/MEG. synchronization and resynchronization: basic principles. *Clin. Neurophysiol.*, 110:1842–1867, 1999.

[52] W. H. Press, B. P. Flannery, S. A. Teukolsky, and W. T. Vetterling. *Numerical Recipes in C : The Art of Scientific Computing*. Cambridge University Press, 2nd edition, 1992.

[53] P. Rappelsberger, G. Pfurtscheller, and O. Filz. Calculation of event-related coherence–a new method to study short-lasting coupling between brain areas. *Brain Topogr.*, 7(2):121–127, 1994.

[54] S. E. Robinson and J. Vrba. Functional neuroimaging by synthetic aperture magnetometry (SAM). Technical report, CTF Systems Inc., Port Coquitlam, BC, Canada, 1998.

[55] S. E. Robinson and J. Vrba. Comparison of SAM and MUSIC performance for unaveraged MEG. In *Biomag 2000, 12th International Conference on Biomagnetism*, Helsinki Univ. of Technology, Espoo, Finland., 2000.

[56] E. Rodriguez, N. George, J. P. Lachaux, J. Martinerie, B. Renault, and F. J. Varela. Perception's shadow: longdistance synchronization of human brain activity. *Nature*, 397:430–433, February 1999.

[57] R. Saab, M. J. McKeown, L. J. Myers, and R. Abu-Gharbieh. A wavelet based approach for the detection of coupling in EEG signals. In *Proceedings of the 2nd International IEEE EMBS Conference on Neural Engineering*, pages 616–620, Arlington, Virginia, March 2005.

[58] J. Sarvas. Basic mathematical and electromagnetic concepts of the biomagnetic inverse problem. *Phys. Med. Biol.*, 32:11–22, 1987.

[59] K. Sekihara, S. S. Nagarajan, D. Poeppel, A. Marantz, and Y. Miyashita. Reconstructing spatio-temporal activities of neural sources using an MEG vector beamformer technique. *IEEE Trans. Biomed. Eng.*, 48(7):760–771, July 2001.

[60] K. Sekihara, S. S. Nagarajan, D. Poeppel, A. Marantz, and Y. Miyashita. Application of an MEG eigenspace beamformer to reconstructing spatio-temporal activities of neural sources. *Hum Brain Mapp.*, 15:199–215, 2002.

[61] K. Sekihara, S. S. Nagarajan, D. Poeppel, and Y. Miyashita. Timevfrequency meg-music algorithm. *IEEE Trans. Med. Imaging*, 18(1):92–97, January 1999.

[62] K. Sekihara, S. S. Nagarajan, D. Poeppel, S. Miyauchi, N. Fujimaki, H. Koizumi, and Y. Miyashita. Estimating neural sources from each time-frequency component of magnetoencephalographic data. *IEEE Trans. Biomed. Eng.*, 47(5):642–653, May 2000.

[63] Kensuke Sekihara, S. S. Nagarajan, D. Poeppel, S. Miyauchi, N. Fujimaki, H. Koizumi, and Y. Miyashita. Estimating neural sources from each time-frequency component of magnetoencephalographic data. *IEEE Trans. Biomed. Eng.*, 47(5):642–653, May 2000.

[64] W. Singer. Striving for coherence. *Nature*, 397:391–393, February 1999.

[65] K. D. Singh, G. R. Barnes, and A. Hillebrand. Group imaging of task-related changes in cortical synchronisation using nonparametric permutation testing. *NeuroImage*, 19:1589–1601, 2003.

[66] M. Sun, S. Qian, X. Yan, S. B. Baumann, X. G. Xia, R. E. Dahl, N. D. Ryan, and R. J. Scalbassi. Localizing functional activity in the brain through time-frequency analysis and synthesis of the EEG. *Proceedings of the IEEE*, 84(9):1302–1311, September 1996.

[67] C. Tallon-Baudry and O. Bertrand. Oscillatory gamma activity in humans and its role in object representation. *Trends Cogn Sci.*, 3(4):151–154, April 1999.

[68] M. Taniguchi, A. Kato, N. Fujita, M. Hirata, H. Tanaka, T. Kihara, H. Ninomiya, N. Hirabuki, H. Nakamura, S. E. Robinson, D. Cheyne, and T. Yoshimine. Movement-related desynchronization of the cerebral cortex studied with spatially filtered magnetoencephalography. *NeuroImage*, 12:298–306, 2000.

[69] J. V. Uspensky. *Theory of Equations*. McGraw-Hill, 1958.

[70] M. Uusitalo and R. Ilmoniemi. Signal-space projection method for separating MEG and EEG into components. *Med. Biol. Eng. Comp.*, 35(2):135–140, March 1997.

[71] F. Varela, J. P. Lachaux, E. Rodriguez, and J. Martinerie. The brainweb: phase synchronization and large-scale integration. *Nat. Rev. Neuro.*, 2:229–239, April 2001.

[72] B. D. Van Veen, W. V. Drongelen, M. Yuchtman, and A. Suzuki. Localization of brain electrical activity via linearly constrained minimum variance spatial filter. *IEEE Trans. Biomed. Eng.*, 44(9):867–879, September 1997.

[73] J. Vrba and S. E. Robinson. Differences between synthetic aperture magnetometry (SAM) and linear beamformers. In *Biomag 2000, 12th International Conference on Biomagnetism*, Helsinki Univ. of Technology, Espoo, Finland., 2000.